DOI:10.14753/SE.2023.2777

NONLINEAR OPTICAL MICROSCOPY FOR THE INVESTIGATION OF SKIN ALTERATIONS IN PSEUDOXANTHOMA ELASTICUM

Ph.D. thesis

Luca Fésűs

Clinical Medicine Doctoral School

Semmelweis University

Supervisor: Norbert Wikonkál, MD, PhD, DSc

Consultant: Róbert Szipőcs, PhD

Official reviewers: Erika Varga, MD, PhD
Barbara Molnár-Érsek, PhD

Complex Examination Committee:
Head: Attila Szijártó, MD, PhD, DSc
Members: Zsuzsanna Szalai, MD, PhD
Krisztina Hagymási, MD, PhD

Budapest

2022

DOI:10.14753/SE.2023.2777

Table of Contents

DOI:10.14753/SE.2023.2777

DOI:10.14753/SE.2023.2777

List of Abbreviations

μm	Micrometer
2D	Two-dimensional
2P	Two-photon
3D	Three-dimensional
BCC	Basal cell cancer
CARS	Coherent anti-Stokes Raman scattering
FAD	Flavin adenine dinucleotide (oxidized form)
FLIM	Fluorescence-lifetime imaging
fs	Femtosecond
Hz	Hertz
HFUS	High frequency ultrasound
H&E	Hematoxilin and eosin
MPM	Multiphoton microscopy
mW	Milliwatt
NAD(P)H	Nicotinamide adenine dinucleotide (phosphate) (reduced form)
NLM	Nonlinear microscopy
OCT	Optical coherence tomography
PXE	Pseudoxanthoma elasticum
RCM	Reflectance confocal microscopy
SHG	Second-harmonic generation
THG	Third-harmonic generation
TPEF	Two-photon excitation fluorescence
Ti:S	Titan-sapphire

DOI:10.14753/SE.2023.2777

1. Introduction

Skin diseases account for 22,5-26,5% of primary care visits worldwide, so basic knowledge of dermatology is extremely important in general practice [1, 2]. The work of a dermatologist has always relied heavily on visual observation of the skin. In the 19th and 20th century, dermatopathology and microscopic examination of histological skin sections became the gold standard for diagnosis of a wide range of dermatological conditions [3]. However, in the 21th century, this is rapidly changing due to an incredible development of imaging techniques in medicine. New modalities have to meet the requirements of dermatological needs, and are expected to offer additional benefits, such as deeper penetration, high spatial resolution, chemical or optical contrast, compared to traditional histopathology [4]. Also, there is an emerging need for noninvasive diagnostic tools, beyond than the classic dermoscope, a simple hand-held microscope, which is the only noninvasive diagnostic device in the daily clinical practice for the time being [5]. New techniques are expected to result in devices that are easy to use, mobile, easy to handle and the clinicians need little training [6]. Besides, economical benefit is an aspect to be considered, as these equipments and instruments will only be implemented into healthcare providers if they are sufficiently cost efficient [7].

1.1 Nonlinear optical processes

1.1.1 A brief overview

Nonlinear optical (NLO) processes were first experimentally demonstrated by P. Franken in 1961, who generated blue light by focusing ruby laser pulses into a quartz crystal [8]. Nonlinear optical phenomena are the basis of many key technologies used today in optical information processing, ultrafast pulsed lasers, optical computers, sensors, laser amplifiers and many others [9]. During electromagnetic wave – matter interactions, the material responses to the incident electric field (E) with induced polarization (P). Conventionally, in linear optics, P is linearly proportional to E, and the frequency of oscillation of the polarization and that of the driving field is the same. This linear polarization explains linear optical events, such as linear absorption - a light wave of a certain frequency that interacts with a molecule might be absorbed and later emitted as a fluorescent light -, it might induce polarization of the same optical frequency (linear polarization), that explains the refractive index of a material [10, 11]. If the intensity of the

light source is sufficient enough to create high peak intensities in the focal point, multiple photons will be absorbed by the material simultaneously, and optical properties of the material will be modified in such a way, that the dependence of P will be non-linear to the strength of the applied optical field. This gives rise to nonlinear optical phenomena [8]. The material response can be described with the Taylor-series expansion [12]:

$$P=\varepsilon_0 [\chi^{(1)}E + \chi^{(2)}E^2 + \chi^{(3)}E^3 + \ldots] = P^{(1)} + P^{(2)} + P^{(3)} = P^{(1)} + P_{non\text{-}linear} = P_{linear} + P_{non\text{-}linear},$$

where $\chi^{(n)}$ is a constant and describes the n^{th} order susceptibility. $P_{non\text{-}linear}$ differs from the linear term as the frequency of the oscillation will be different from that of the incident light, and new frequency components, called harmonics appear [13]. However, to generate these new terms at significant rates, very high electric field is required [14]. Although scientists met with NLO phenomena in relation to the appearance of lasers, high E is typically generated ultrafast - pico- or femtosecond - laser pulses which produce very high peak intensities in the focal volume of 0,1 femtoliter. The lower the frequency of the laser pulses, the higher the probability of NLO events, besides low average laser output power [15]. NLO imaging techniques give the contrast of imaging through the interaction of the light and medium.

As the NLO processes are only rise in the focal point through optical focusing, imaging is not disturbed by light scattering, and unprecedented resolution is enabled [16]. Besides, low average powers ensure negligible phototoxicity and thermal damage [17, 18]. NLO imaging offers solution to medical challenges ranging from molecular-level studies to clinical investigation of patients. The most important nonlinear optical effects with medical application are two-photon excitation fluorescence (TPEF), second harmonic generation (SHG), third harmonic generation (THG), Coherent anti-Stokes Raman scattering (CARS) and stimulated Raman scattering, (SRS). These modalities are also called as multiphoton processes, as two or three photons interact with the other at a time [19]. Most significant advantage of NLO imaging techniques is that there is no need for stains or labeling, as detectable emitted signal is created by the excitation of the molecules [20]. The integration of NLO imaging in microscope systems led to the appearance of nonlinear optical microscopy (NLM) or multiphoton microscopy (MPM). NLM applications in medical and dermatological research is already ongoing. As several molecule in the skin acts as an endogenous cromophores, *in vivo* imaging is also feasible

[21]. See Table 1. for the excitation and emission spectra of these chromophores and other molecules and chemical bonds that are subject to NLM imaging in the skin.

Table 1. Endogenous chromophores in the skin

Chromophore	**Two-photon Excitation λ_{ex} (nm)**
Fluorescence and SHG	
Retinol [19]	700–830
NADH [19]	690–730
Flavins [19]	700–730
Elastin [19]	700–740
Collagen	
Fluorescence [21]	700–740
SHG [22]	700-900

NLM provides spatial resolution is in the sub-micrometer range, and high temporal resolution enables the follow-up of physiological processes *in vivo*. Parallel imaging of distinct molecules and structures can be visualized in multicolor pictures, and 3 dimensional (3D) outputs can also be aquired if we capture images in multiple depths. Compared to other *in vivo* imaging techniques already in the clinical practice, NLM provides higher resolution and selective imaging compared to optical coherence tomography (OCT) and enables deeper penetration as opposed to reflectance confocal microscopy (RCM) [23, 24]. TPEF, SHG and CARS imaging is already used for *in vivo* imaging of the skin and available in the market as a device named MPTflex and MPTflex-CARS [25]. However, costs are currently much higher than that of RCM, and diagnostic quality does not exceed RCM, thus, until now, mostly experimental results are available [26].

1.1.2 Two-photon excitation fluorescence

DOI:10.14753/SE.2023.2777

During TPEF two photons excite a molecule simultaneously (within 0,5 fs apart) into a higher-energy state, where the energy is equal to the sum of the photon energies. Thus, the emitted photon energy will be higher than that of the incident photon (Figure 1A). In case of TPEF, the absorbed power and the emitted signal intensity is proportional to the square of the input power [27, 28]. Fluorophores in the skin, which can be detected and visualized by TPEF are keratin, melanin, elastin, nicotinamide adenin dinucleotide + hydrogen (NADH) and flavin adenin dinucleotide (FAD) [29]. Additional atoms or molecules can also be excited, where a single photon energy would not be sufficient. Moreover, despite the exciting laser beam operates in the near infrared (NIR) range and penetrates deeper in the skin, the emitted higher-energy photon falls into the visible range of the electromagnetic spectrum, and can be detected with bandpass filters of different wavelength range [30].

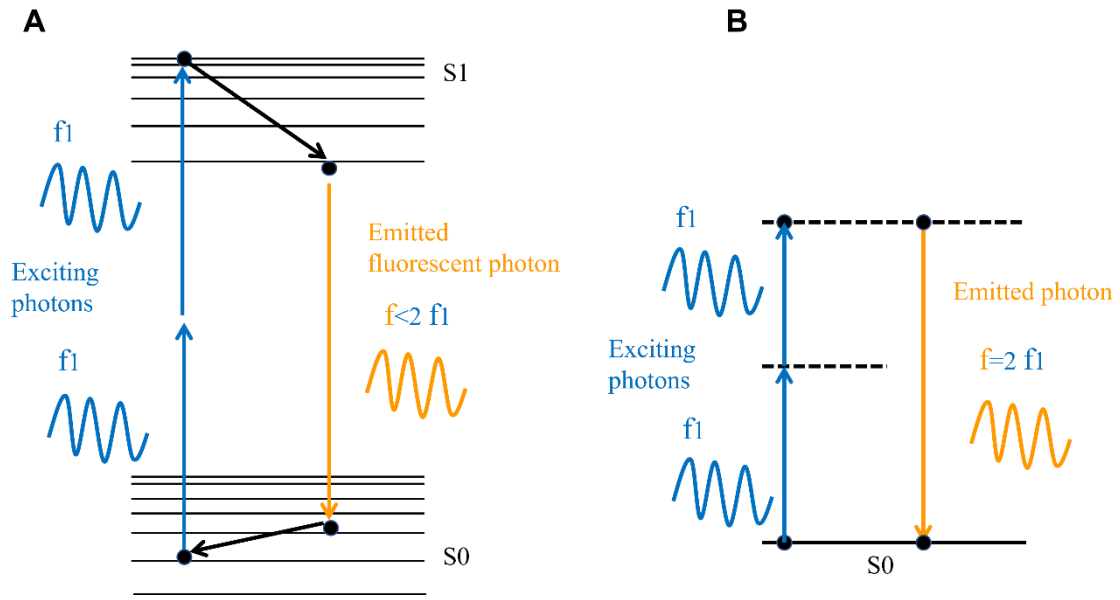

Figure 1. Mechanism of the introduced nonlinear optical phenomena. (A) Two-photon excitation fluorescence. Two incident photons with the same frequency is absorbed by the molecule, that reaches a higher energy state. After a non-radiating deexcitation, a fluorescent photon is emitted and the electrons return to ground state. (B) Second harmonic generation. This phenomenon occurs in materials that lack inversion symmetry and exhibit high spatial orientation. The two incident photons with the same frequency are not absorbed, but combined. Their energy is conserved, and the frequency of the emitted photon will be the double of the initial photons.

1.1.3 Second-harmonic generation

Materials that lack inversion symmetry can exhibit $\chi^{(2)}$ nonlinearity [31]. In this case, two photons interact with a material, and they are not absorbed, but scattered, and energy of the emitted photon will be twice of the incident photons without any energy loss (Figure 1B). As the generated new term is a wave with twice the optical frequency of the incident photon, this phenomenon is also called as frequency doubling, where the phase-matching requires $n(\omega)= n(2\omega)$ [32, 33]. The intensity of the emitted SHG signal is proportional to the square of the input power [34]. Such non-centrosymmetric macromolecules are the collagen, tubulin and myosin [35, 36]. In the skin, collagen gives rise to an intense SHG signal, so skin diseases that affect structure, amount or organization of collagen can be investigated with this modality [37]. During TPEF and SHG imaging, one tunable, mode-locked laser light source is used. A tunable laser wavelength can be set to match the excitation wavelength of the molecule to be examined, whereas mode-locking provides pico- or femtosecond laser impulses instead of a continuous wave light source [38]. This latter parameter is preferable during *in vivo* applications, as the possibility of thermal damage becomes lower [39]. Currently, ultrashort tunable laser pulses produced by broadband Titanium-sapphire (Ti:Sa) being used for TPEF or SHG imaging [28, 40]. Lately, these solid-state lasers are also paired with optical fibers, that might transmit the laser beam to the investigated material and also the emitted optical signal [41]. This technique founds the future use of NLM in clinical practice or in the field of endoscopy [42].

1.1.4 Dermatological applications of nonlinear optical imaging

A combination of these modalities is a commonly found in commercially available NLO systems. The first multimodal multiphoton microscope with CE mark was DermaInspect introduced in 2003 (JenLab GmbH, Germany), capable of TPEF and SHG imaging [43]. Next, the first fibre-coupled microscope system appeared in 2009, that could carry out TPEF, SHG and CARS imaging [44]. In 2010, JenLab created a multiphoton tomography device with flexible arm, called MPTflex [45, 46, 47]. Although substantial progress has been made in this device with its improved resolution compared to OCT and RCM, *in vivo* reports show that the imaging depth that still provides cellular resolution is only up to 100 μm. However, detection of different nonlinear optical signals of simultaneously excited molecules enable multicolor images [25]. Still, the cost of the installation and operation of NLM exceeds that of RCM, whereas it lacks additional benefits. Thus, the use of NLM

is rather profitable in research institutions, and we still have to wait for its implementation in general patient care [48]. In dermatological basic science, NLM is widely used to monitor connective tissue alterations of the skin during aging, photoaging [49, 50, 51, 52]. Also, transdermal penetration of various compunds found in cosmetic products was also investigated [53, 54, 55, 56, 57]. In clinical studies, *ex vivo* NLM was used to examine rare connective tissue diseases of genetic origin [58, 59]. *In vivo* studies are available, but these were done in a limited number of patients. A sensitivity of 84,8% and specificity of 100% was found in the diagnosis of basal cell cancer [60]. *In vivo* imaging of basal cell cancer was investigated with MPTflex in 9 patients, where basaloid cell nests were recognized on the MPM images, and palisading was recognized in some areas. Cellular resolution of deeper nests was a limitation of this study, where signal to noise ratio significantly decreased. This hampers its application possibilities in the case of invasive cancer subtypes [22]. NLM was also suitable to diagnose and differentiate squamous cell cancer from its premalignant stage, actinic keratosis [53, 61]. In the examination of melanocytic lesions, sensitivity was 71-76% and specificity was 72-97%. The i*n vivo* diagnosis of melanoma, both sensitivity and specificity was at least 95% [54, 62, 63]. Besides malignant skin lesions, several other skin conditions were studied, and now we are more familiar with nonlinear microscopic features of inflammatory skin conditions, such as atopic dermatitis or psoriasis [25], autoimmune bullous diseases, seborrheic keratoses *in vivo* [64].

1.1.5 Spectral decomposition

A common challenge that arises during NLO imaging, is the overlapping emission spectra of the investigated components, that result in poor signal to noise ratio. Thus, multispectral aquisition and spectral unmixing is necessary to determine the relative amount of the fluorophores. These information yield in the chemical composition of the sample on a submicrometer scale [65, 66]. Multidimensional vectoral spaces are often used to describe spectral distribution of light reflected from different targets in multispectral remote sensing applications using satellites [67], which are based on predefined color bands (bandpass filters) as base vectors. Depending on the number of investigated fluorophores, multiple excitation wavelengths and emission filters are required together with several regions imaged throughout the sample. In general, the number of separate spectral channels has to be at least the number of components that are measured. The applied emission filters also have to best match their emission spectra. Analysis of the results

involves complex mathematical approaches [68]. In medical research, hyperspectral or multispectral unmixing separates structures with similar spectrum from other regions based on their spectral characteristics. As a noninvasive alternative to histologic staining, here an “optical staining” is created, that provides histological tissue information and morphological data in a rapid, non-destructive way [69].

Overall, these NLO techniques are suitable for both *ex vivo* and *in vivo* investigation of the skin in 2- or 3D. Combination of these methods results in multimodal imaging, while the application of several excitation or emission spectrum leads to multispectral imaging. In dermatology, TPEF is usually used together with SHG to provide information about keratin, elastin and collagen and to visualize both the epidermis and dermis. With NLM, we can investigate skin cancers, inflammatory skin disorders, the effect of metabolic diseases, genetic skin diseases, and also skin aging [70]. Our research group previously utilized NLM for the *ex vivo* detection of basal cell cancer [71], for *in vivo* assessment of connective tissue alterations of the dermis in murine models [70, 72] and for *ex vivo* investigation of rare genetic diseases with skin involvement [58, 59]. During my research we also worked on the development of a NLM setup capable of CARS imaging to detect basal cell cancer in a stain-free noninvasive way on *ex vivo* skin biopsies [73], and we studied collagen fibre structure of basal cell cancer tumor nests with SHG on *ex vivo* skin sections [74]. Given the stain-free optical imaging features of NLO imaging, it may serve as an *in vivo* alternative of the gold standard of diagnosis, histopathology in the future.

1.2 Pseudoxanthoma elasticum

Pseudoxanthoma elasticum (PXE, OMIM#264800) is a rare, multisystemic, metabolic disease that is characterized by ectopic mineralization of soft connective tissue [75]. The etimology refers to the cutaneous alterations resembling xanthomas, together with the involvement of elastic fibers. Skin, eyes and the cardiovascular system are the organs most often affected, and clinical manifestations show progression with life that leads to peripheral arterial disease, stroke or blindness [76]. There are only estimations to the prevalence due to the often subtle visible skin alterations, and diagnosis is usually made only after severe complications. The current incidence of diagnosed cases varies between 1:25000 – 1:100000 [77] and women are twice often affected [78]. Carrier frequency is reported to be about 1 per 100 [79].

1.2.1 Etiology

Until the 21th century, there were only theories about the pathomechanism of PXE. In 2000, research groups identified mutations in the *ATP-binding casette sub-family C member 6 (ABCC6)* gene (OMIM#603234) in the background of PXE. Although the exact mechanism of ectopic mineralization was not revealed back then [76]. In the upcoming years, researches stated that PXE is caused by an unknown factor in the circulation, that requires ABCC6, rather that by the lack of ABCC6 as expected earlier. In 2013, *Jansen et al.* proved this circulating factor to be the inorganic pyrophosphate (PPi). They showed, that ABCC6 indirectly raises plasma PPi levels via the excretion of ATP and other nucleosid triphosphates [80]. Although the mode of ATP transportation is yet unclear, hepatocytes release ATP in an ABCC6-dependent manner, that is instantly converted into AMP and PPi by plasma ectonucleotidases (ENPPs). Loss-of-function mutations of the *ABCC6* gene is the most common cause of PXE, although other mutations have also been described [81]. In case of a defective ABCC6 protein, a reduced level of plasma PPi and reduced pyrophosphate/phosphate ratio is measured [82]. In line with these findings, PXE patients have significantly lower amount of plasma PPi compared to healthy individuals [82]. PPi is known as an anti-mineralization factor that inhibits hydroxyapatite crystal deposition [83]. Unlike ATP, systemic PPi has higher plasma half-life that ensures a sufficient systemic concentration, peripheral activity and inhibition of ectopic mineralization [82]. Low plasma levels of PPi and reduced pyrophosphate/phosphate ratio

is likely contribute to aberrant ectopic mineralization [84]. Recently, reduced plasma PPi levels were also claimed in other diseases with ectopic mineralization [85].

1.2.2 Clinical presentation

Cutaneous manifestations tipically develop in childhood or adolescence. The apperance of small yellowish papules on the lateral aspects of the neck is usually the first sign of PXE. Later, papules develop in flexural areas, coalesce into reticulated plaques and give the skin a cobblestone-like appearance [75]. Mucosa may also be affected. Later, the skin becomes wrinkled and redundant skin folds appear in the axillae, groin and abdominal area, that lead to severe aesthetic impairment [86]. Ophthalmologic manifestations are the result of calcification of the elastic fibres in the choroideal Bruch's membrane. Drusen-like pigmented dark spots, called „peau d'orange" in the temporal region of the posterior pole are early signs. Then, mineralization leads to cracks in the membrane, that will manifest as angioid streaks [87, 88]. This triggers neovascularization, leading to subretinal hemorrhage and progressive loss of central vision [75]. Cardiovascular involvements are the consequence of early atherosclerosis due to mineralization of the elastic fibers in the internal elastic lamina of the vessels. This medial arterial calcification is also referred to as arteriosclerosis, that affects vessels of the extremities, coronary arteries, and the cerebral circulation [89]. Early acute myocardial infarction, gastrointestinal bleeding and stroke may also develop [86]. A clinical scoring system was proposed by *Legrand et al.* [90] to estimate disease severity, shown in Table 2. Eye and cardiovascular manifestations appear several years after the onset of skin lesions, and the severity of ophthalmological symptoms was shown to correlate with the severity of skin lesions [91]. However, ocular or vascular manifestations may also evolve in the absence of skin changes [92].

Table 2. Severity scoring system proposed by *Legrand et al.*, that is an extended version of the Phenodex standardized scoring system to evaluate PXE patients [90].

Organ system findings	
Skin	
S0	No sign
S1	Papules/bumps
S2	Plaques of coalesced papules
S3	Lax and redundant skin
Eye	
E0	No sign
E1	*Peau d'orange*
E2	Angioid streaks
E3	Bleeding and/or scarring
Gastrointestinal	
G0	No sign
G1	Gastrointestinal bleeding as related to PXE
Vascular	
V0	No sign
V1	Weak or absent pulse or peripheral artery disease revealed by vascular imaging
V2	Intermittent claudication
V3	Vascular surgery or Stroke/TIA
Cardiac	
C0	No sign
C1	Chest pain/angina/abnormal EKG or abnormal stress test with no symptom, or Mitral insufficiency
C2	Heart attack
Renal	
R0	No sign
R1	Nephrolithiasis

1.2.3 Diagnosis

Although there were earlier attempts to describe the criteria of PXE back in the 1970s, diagnostic and classification criteria kept constantly changing as the diagnostic tools developed [92]. The latest proposal for diagnosis and classification of PXE was presented by Plomp *et al.* in 2010, who incorporated molecular genetic findings in the guidelines. According to this update, dermatological, opthalmological and molecular genetic examination is necessary, and clinical findings solely are not sufficient to confirm PXE [88]. This approach classifies PXE patients into „definite", „probable" and „possible" categories, based on the major and minor criteria they fulfill (Table 3).

Besides clinical findings, skin biopsy and/or mutational analysis is required for diagnosis. For histopathological examination, specific stains are used besides hematoxilin and eosin (H&E). Weigert's elastic (WE) staining or elastic van Gieson (VG) stain show fragmented elastic fibres, and von Kossa (VK) staining is used to highligh mineral deposition [93]. Skin histopathology reveals alterations in the mid-dermis, whereas the papillary dermis and deeper layers of the reticular dermis remain unaffected. Characteristic histological features are fragmented, clumped and mineralized elastic fibres, as well as calcium deposits in the mid-dermis. Calcification mainly consists of calcium hydroxyapatite and calcium hydrogen phosphate [94]. Polymorphous, coiled elastic fibers are also visible [94]. In the affected areas, collagen bundles are irregular in diameter and a flower-like cross-sectional shape is apparent in most patients, although these were stated as aspecific changes. Interstingly, histologic alterations are present in skin regions that seem to be unaffected by visual inspection [95]. Ultrastructural studies reveal two types of calcification: fine mineral precipitates deposited in the core of the elastic fibers, and bulky deposits around the fibers, that will lead to their fragmentation [86]. The rarity and considerable inter- and intrafamilial heterogenity in phenotype challenges recognition of PXE and is responsible for an often delayed diagnosis [92, 96, 97].

DOI:10.14753/SE.2023.2777

Table 3. Revised diagnostic criteria for pseudoxanthoma elasticum. Source: *Plomp et al.* 2010 [88].

Major diagnostic criteria
1. Skin
a. Yellowish papules and/or plaques on the lateral side of the neck and/or flexural areas of the body; or
b. Skin biopsy: fragmentation, clumping and calification of elastic fibers
2. Eye
a. Peau d'orange;
b. Angioid streaks (AS) (at least as long as one disk diameter)
3. Genetics
a. Pathogenic mutation of both alleles of the *ABCC6* gene
b. A first degree-relative meeting the diagnostic criteria for definitive PXE
Minor diagnostic criteria
1. Eye
a. One AS shorter than one disk diameter; or
b. One or more 'comets' or 'wing signs' in the retina
2. Genetics
a. Pathogenic mutation of one allele of the *ABCC6* gene
Diagnostic requirements
Definitve diagnosis The presence of ≥ two major criteria of different categories
Probable diagnosis The presence of two major eye or two major skin criteria, or The presence of one major criterion and ≥ one minor criteria not belonging to the same category as the major criterion
Possible diagnosis The presence of a single major criterion, or The presence of ≥ one minor criteria

1.2.4 Therapy

There is yet no successful medical treatment to counteract systemic ectopic mineralization. A number of studies advise dietary considerations. High calcium and phosphate intake should be avoided as it correlated with more severe forms of PXE. Phosphate-low diet and phosphate binders might slow down the progression of the disease according to clinical studies [92]. PPi supplementation was found not to be effective due to its short plasma half-life. Bisphosphonates (BP), however, have been successful in other disorders of mineralization as nonhydrolyzable PPi precursors effective via *per os* administration [80]. A PPi analog etidronate intake also prevented mineralization [75]. Results from animal studies suggest, that another, naturally occurring systemic mineralization inhibitor, α-fetuin may prevent ectopic calcification [86]. Application of small molecular weight compounds that facilitate translational read-through of premature termination codon mutations - which make up a large percent (40%) of mutations – in the *ABCC6* gene, may become new treatment options in the future [86]. Chaperone molecules were demonstrated to be helpful to correct misfolded or mistargeted proteins *in vitro*. Cell transplantation from hepatoblastic cell lines is another cell-based strategy [92]. Vector transferred and plasmid based gene therapy are subject to intensive research [75].

Skin alterations are usually corrected with cosmetic surgical interventions [98, 99]. Today, for the eye complications anti-vascular endothelial growth factor (anti-VEGF) treatment replaced invasive treatments – such as laser photocoagulation, transpupillary thermotherapy and photodynamic therapy - and it shows superior efficacy to control choroidal neovascularization [92]. To prevent cardiovascular complications, a general, but more agressive approach to healthy lifestyle is expected from patients. Cessation of smoking, cholesterol-lowering agents, physical excercise are advised to prevent accelerated atherosclerosis [75].

DOI:10.14753/SE.2023.2777

2. Objectives

Calcium deposits, a histopathological hallmark of PXE could not be visualized so far with NLM. Data in literature regarding the examination of skin alterations and its association with systemic complications in PXE is still controversial and rather scarce for the latter. There is yet no biomarker that would anticipate the natural flow of the disease in individual patients. This unexplored field originates from the rarity of the disease, the usually late onset of symptoms, the underdiagnosis of PXE and the lack of multidisciplinary cohort studies. Moreover, an imaging device and methodology to visualize fine alterations of elastic fibers and mineral deposits in the skin is yet to be developed and tested. Our group utilized an NLO imaging apparatus capable of simultaneous TPEF and SHG imaging. In an attempt to clarify some of above problems, we conducted these experiments and aimed to answer the following questions:

2.1 I. Experiment: To utilize *ex vivo* TPEF and SHG imaging in PXE

1. Is *ex vivo* NLM suitable to visualize histopathological alterations of elastin and collagen, and reveal calcium deposits in PXE skin sections orthogonal to the skin surface with TPEF and SHG techniques?

2. Do quantitative parameters of elastin and collagen fibres differ between healthy controls and PXE patients?

3. How variable is the extent of calcification in the mid-dermis? Does this correlate with a possible soluble biomarker, PPi?

2.2 II. Experiment: To carry out spectral decomposition on *ex vivo* NLM images of PXE skin sections

1. Is Phloxine B staining suitable to create optical contrast between TPEF signal of elastin and calcification of deparaffinized PXE skin sections?
2. Is it possible to spectrally separate collagen, elastin and calcification with mathematical algorithms, when three different bandpass filters are used to capture TPEF and SHG signals to create concentration maps of these tissue components and multicolor images of PXE sections?

DOI:10.14753/SE.2023.2777

3. Results

Pulications that were used for the thesis:

Fésűs L, Plázár D, Kolonics A, Martin L, Wikonkál N, Medvecz M, Szipőcs R**.** Low concentration Phloxine B staining for high chemical contrast, nonlinear microscope mosaic imaging of skin alterations in pseudoxanthoma elasticum. Biomedical Optics Express. 2022 13(1): 252-61

Kiss N, **Fésűs L**, Bozsányi S, Szeri F, Van Gils M, SzaboóV, Nagy AI, Hidvegi B, Szipőcs R, Martin L, Vanakker O, Arányi T, Merkely B, Wikonkál NM, Medvecz M**.** Nonlinear optical microscopy is a novel tool for the analysis of cutaneous alterations in pseudoxanthoma elasticum. Lasers Med Sci. 2020 35(8): 1821-30

Ethics approval:

Our present studies were approved by the Semmelweis University Regional and Institutional Committee of Science and Research Ethics, Budapest, Hungary (SE TUKEB no. 193/2017 and SE RKEB no. 193-2/2017).

3.1 I. Experiment

3.1.1 Phenotype

Five patients were included in this study, three of them were female. Their mean age was 53.8 ± 11.7 years. Three female and two male healthy individuals were involved in the study as controls. Their mean age was 52.2 ± 4.9 years. None of the patients were absent of skin, eye and vascular complications. We found cardiac alteration in one patient. No gastrointestinal or renal disease was observed. Clinical pictures of skin alterations of PXE patients are shown in Figure 2. Plasma PPi levels were significantly lower in PXE compared to healthy controls (mean ± SD 0.232 ± 0.063 μM vs 0.947 ± 0.108 μM) (Figure 3).

DOI:10.14753/SE.2023.2777

Figure 2. Clinical pictures of affected skin areas of the five PXE patients. Pt: Patient. Pt1: yellowish papules on the neck, wrist and axilla. Pt2: yellowish papules on the neck. Pt3: yellowish papules on the neck and groin. Pt4: coalescing yellowish plaques on the neck, papules on the wrist and redundant skin folds in the axilla. Pt5: yellowish papules on the neck and redundant skin folds in the axilla.

DOI:10.14753/SE.2023.2777

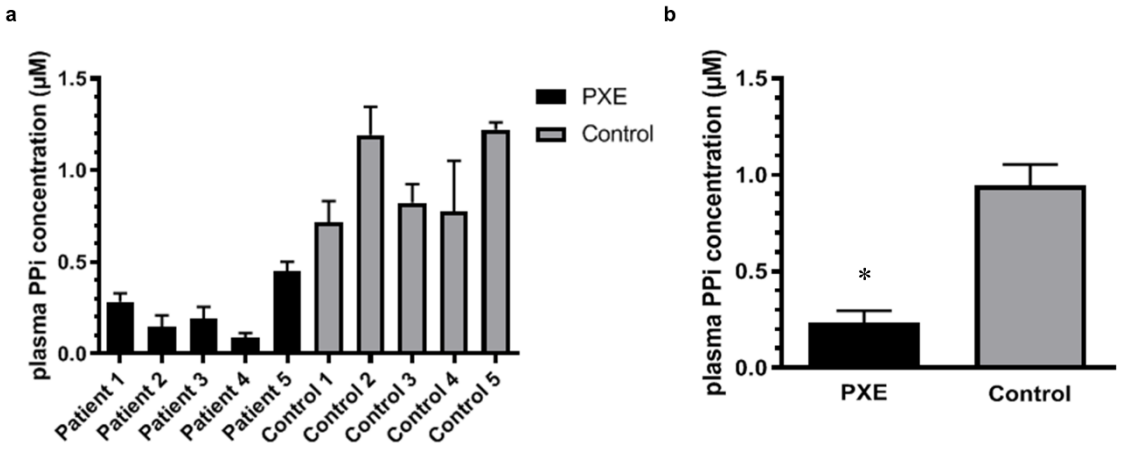

Figure 3. Plasma inorganic pyrophosphate (PPi) levels of the PXE patients compared with age- and gender-matched healthy controls. Blood samples were collected and platelet-free plasma was prepared. a.) To determine plasma PPi levels of all included patients, first, PPi was converted to ATP by an enzymatic method, then ATP content was measured by a bioluminescent assay. Plasma PPi concentration was calculated based on calibration standards and corrected for initial plasma ATP concentration. b.) Plasma PPi levels in PXE vs control patients were compared using unpaired Student's t test. *$p < 0.05$. Pt, patient; Co, control [100]

3.1.2 Histopathologic examination

We found the epidermis, the papillary dermis and the deep dermis to be morphologically normal both in controls and PXE patients. However, we found marked alterations in the mid-dermis of PXE patients. H&E staining displayed polymorphous, shredded elastic fibers and fibroblasts (Figure 4). WE staining showed irregular, clumped and mineralized elastic fibers. With VK staining, mid-dermal mineral deposits and calcified elastin fiber fragments were revealed. Lastly, VG staining showed disrupted collagen fibers oriented around the calcium deposits. All these features were absent in healthy controls.

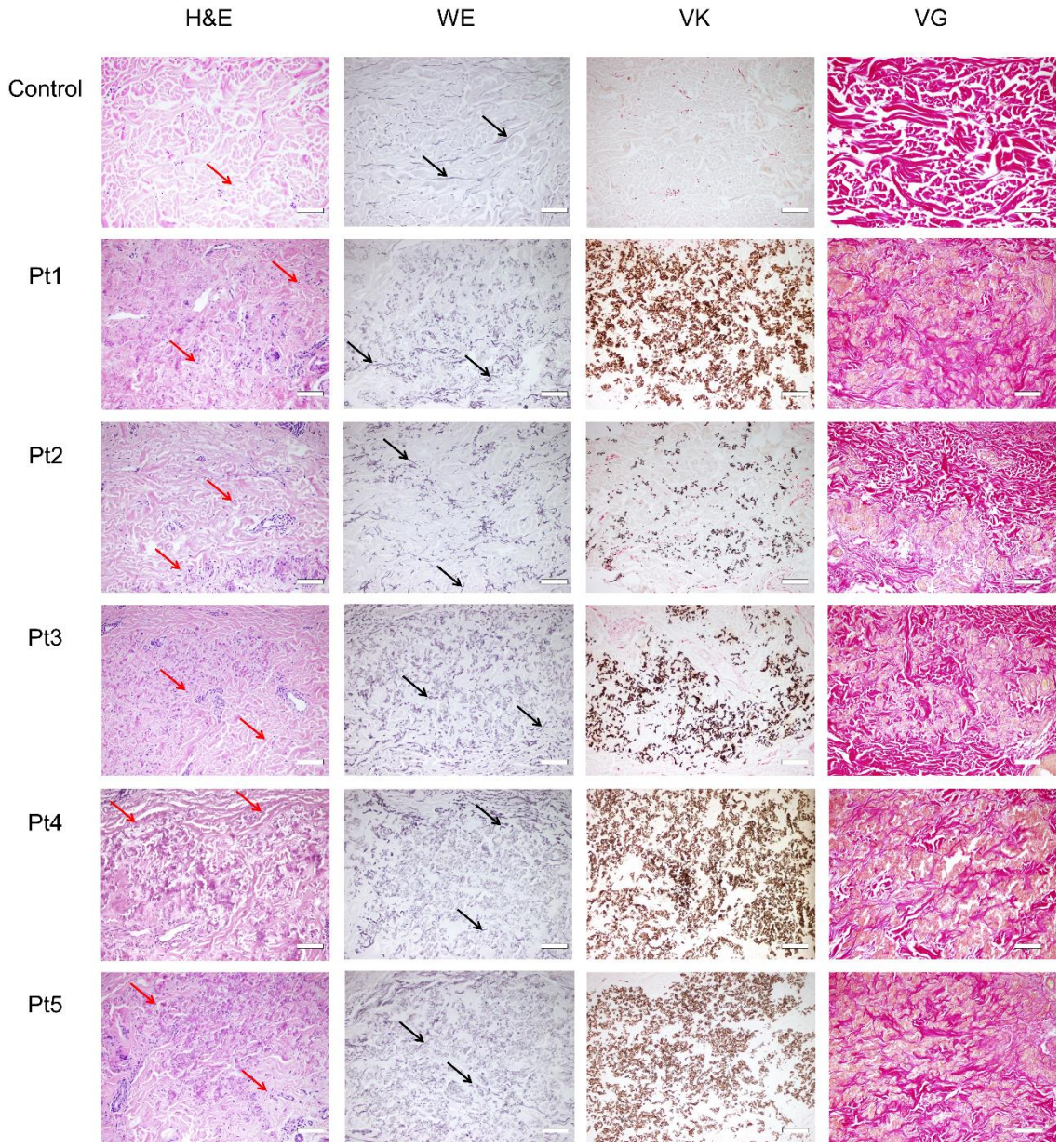

Figure 4. Representative histology images of the mid-dermis of healthy and PXE-affected skin, stained with hematoxylin and eosin (H&E), Weigert's elastic (WE), von Kossa (VK), and Van Gieson's (VG) stains. Red arrows, fibroblasts; black arrows, elastic fibers. Scale bars display 200 μm. Pt, patient [100]

3.1.3 Nonlinear optical microscope imaging

Two-channel NLO microscope mosaic images of healthy and PXE-affected skin sections orthogonal to the skin surface are shown in Figure 5. Similarly to the histological findings, the epidermis, papillary dermis and deep dermis were unaffected in all patients. In healthy

controls, we saw intact elastic fiber network in the TPEF channel and interwoven collagen bundles in the SHG channel in the mid-dermis. On the contrary, mid-dermis of PXE patients consisted of discrete or confluent masses of calcium deposits, surrounded by mineralized, broadened and fragmented elastic fibers in the green TPEF channel (Figure 5). The number of elastic fibers in the mid-dermis (see right panel of Figure 6a) in PXE patients was found to be significantly increased in PXE patients compared to controls (175.7 ± 79.49 vs 97.56 ± 29.30). Elastic fiber length was significantly lower in PXE, than in healthy subjects (59.49 ± 0.66 μm vs 91.64 ± 5.6 μm) (Figure 6b). We did not detect any calcification in controls. Although calcification was present in the mid-dermis of every PXE patient, we found a considerable variation in the outlined relative surface area of calcium deposits (see Figure 6c) among them. Relative surface area of calcification was compared with plasma PPi levels, but no correlation was found (data not shown). In the SHG channel of PXE skin sections, irregularly shaped collagen fibers were visible (see Figure 5). Analyzation of collagen fiber lenght and width with the CT-FIRE software revealed significantly shorter collagen fiber length (67.99 ± 0.79 μm vs 73.53 ± 1.04 μm) and fiber width (6.8 ± 0.06 μm vs 7.33 ± 0.07 μm) in PXE skin sections compared to controls (Figure 6d,e), although the difference in the absolute values is clinically not considerable.

DOI:10.14753/SE.2023.2777

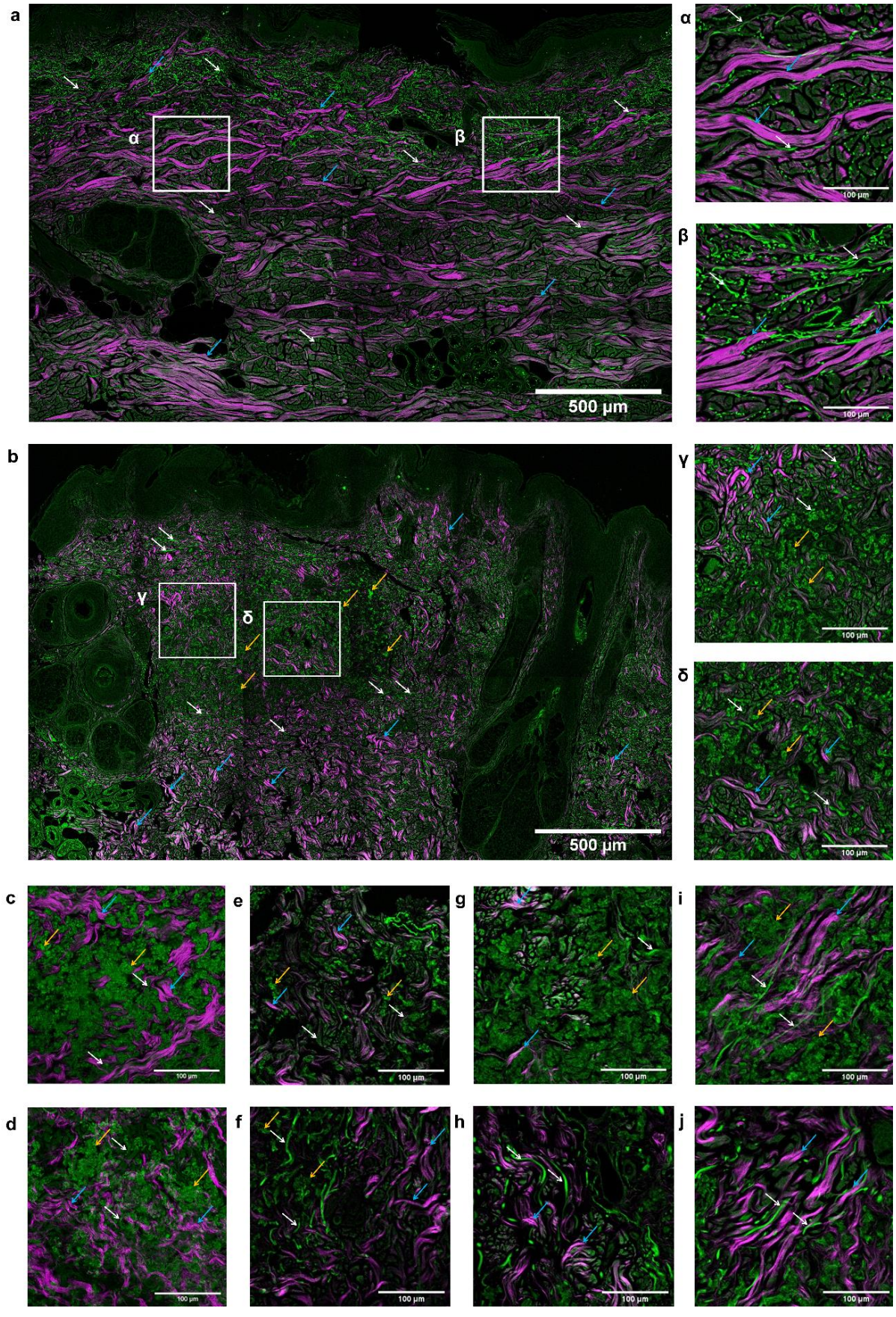

100

Figure 5. Two-photon excitation fluorescence (TPEF) and second-harmonic generation (SHG) images of PXE-affected and healthy skin sections orthogonal to the skin surface. TPEF signal (green) is mainly emitted by elastin and calcification in the dermis, although keratin also emits TPEF photons. SHG (magenta) displays the collagen network. Ti:Sa laser was operated at 800-nm excitation wavelength. 420 × 420 μm^2 frames were captured along the x, y plane and assembled into mosaic images (a, b). a) Control skin, b) skin sample from PXE patient 3. Representative areas from the mid-dermis indicated with white squares highlighted and magnified (α, β, γ, δ). α, β) healthy control, γ, δ) patient 3. Representative 300 × 300 μm^2 images with higher magnification of the mid-dermis from patients 1, 2, 4 and 5(and c–j). c, d) patient 1, e, f) patient 2, g, h) patient 4, i, j) patient 5. White arrows, elastin fibers; blue arrows, collagen fibers; yellow arrows, calcium deposits. Scale bars display 500 μm for mosaic images and 100 μm for high magnification images [112].

DOI:10.14753/SE.2023.2777

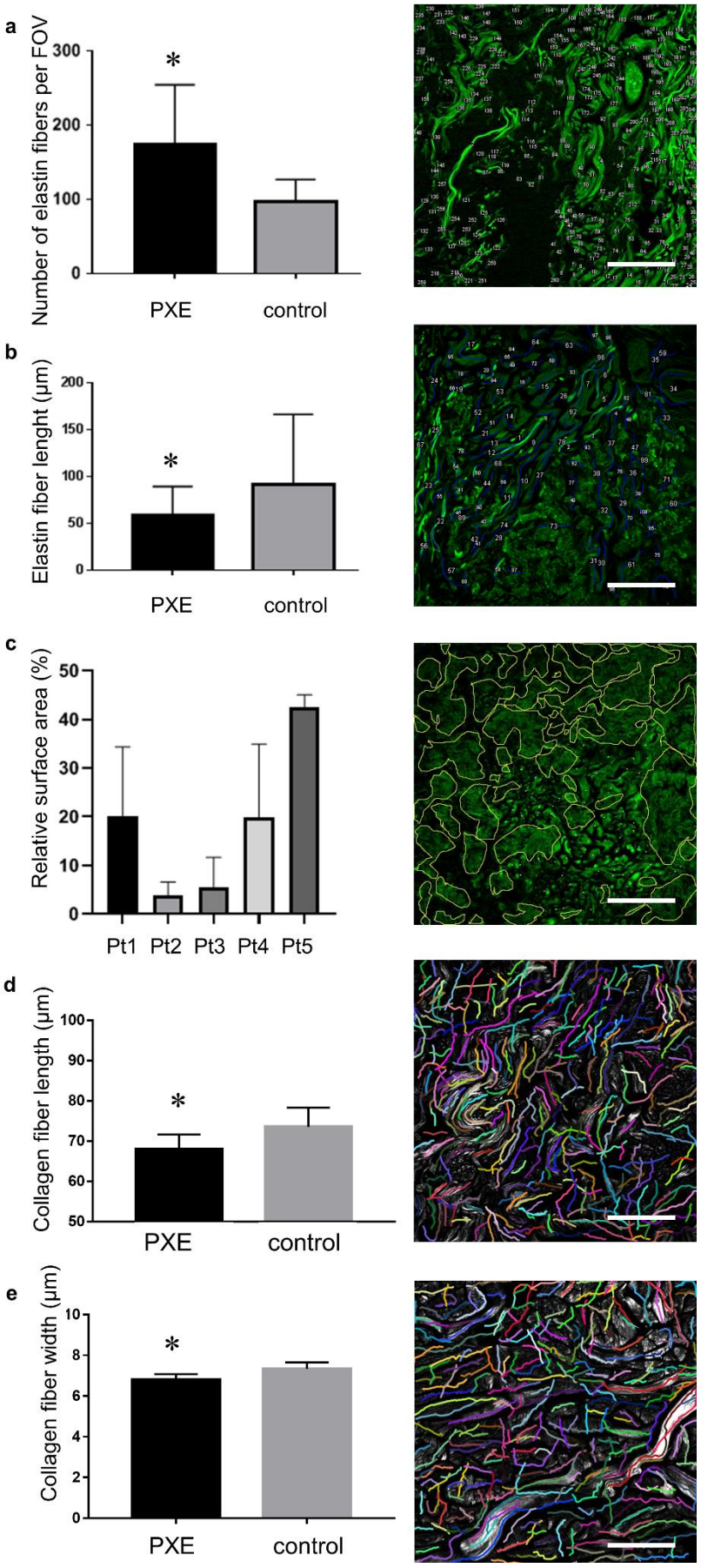

Figure 6. Quantitative analysis of elastin, cacification and collagen in PXE patients and healthy controls. Number of elastin fibers was manually counted and their lenght was assessed in a semi-automated way in raw two-photon excitation fluorescence (TPEF) images from the mid-dermis of PXE patients and controls. Extent of calcification was estimated on TPEF images by manual outlining of the calcium deposits and a relative surface area was calculated. The ImageJ software was used for these operations. Collagen fiber lenght and width was analysed by the CT-FIRE software ran on raw second-harmonic generation (SHG) images from the mid-dermis of PXE-affected and control skin. For all analysis, 10 representative field of views were included in each group. a) Number of elastin fibers in PXE vs control patients (mean ± SD 175.7 ± 79.49 μm vs 106.8 ± 23.92 μm), b) length of elastin fibers in PXE vs control patients (59.49 ± 29.9 μm vs 91.64 ± 74.72 μm), c) relative calcification surface area in each PXE patient. Right panels show representative TPEF images from PXE samples for each parameter. Statistical analyses were carried out with the Mann-Whitney U test. e, f) Collagen fiber length (mean ± SD 67.99 ± 3.612 μm vs 73.53 ± 4.782 μm) (e) and width (6.797 ± 0.274 μm vs 7.327 ± 0.325 μm) (f) were compared with Student's t test after customized CT-FIRE analysis of raw SHG images. Representative images of CT-FIRE v.13 (LOCI, University of Wisconsin – Madison, WI, USA) analysis of patient 1 and a healthy control. Scale bars display 100 μm. *$p < 0.05$ [100]

3.2 II. Experiment

3.2.1 Vectorial representation of nonlinear optical signals

Gain-normalized nonlinear optical signal levels for each tissue component – collagen, elastin and calcification - in different detection channels is summarized in Table 4. for a PXE cryosection (left) and for the Phloxine B stained, deparaffinized sections (right). For the latter, data is expressed as mean and standard deviation. These normalized signal values were used to visualize optical emission spectra from the three examined tissue components in a 3D vectorial space.

Table 4. Color vector values describing gain-normalized signal intensities of collagen, elastin and calcification in the PXE cryosection and Phloxine B stained PXE sections. Vectorial endpoint coordinates are determined by values in the three detection channels

supplied with bandpass filters 405/20 (magenta, SHG), 460/50 (cyan, TPEF) and 590/45 (orange, TPEF), respectively. A detection channel is highlighted with its corresponding color, were highest nonlinear optical (SHG or TPEF) signal of the given compound was measured. Data is expressed as mean ± standard deviation for the Phloxine B stained PXE sections [101].

	Fresh-frozen PXE cryosection			**Phloxine B stained PXE sections**		
Detection channel (vector coordinate)	Collagen	Elastin	Calcium deposits	Collagen	Elastin	Calcium deposits
405/20 nm	1,597	0,032	0,028	1,92±0,09	0,13±0,10	0,11±0,05
460/50 nm	0,229	0,671	0,441	0,12±0,02	0,61±0,11	0,38±0,19
590/45 nm	0,108	0,184	0,109	0,36±0,14	0,28±0,10	1,96±0,35

As expected, collagen emitted a strong SHG signal that could be detected in the violet channel both in the cryosection and in the Phloxine B stained sections. On the other hand, collagen emitted low TPEF signal in the cyan and orange detection channels, both in case of the cryosection and Phloxine B stained sections. Elastin and calcification had an extremely low TPEF signal contribution to violet channel. However, both elastin and calcification exhibited a broad, overlapping emission spectrum from the cyan, over the green, to the orange (435-610 nm) spectral range in the fresh-frozen PXE section. Color vector representation of gain-normalized nonlinear optical signals revealed, that in the cryosection, direction of color vectors of elastin and calcification are nearly equivalent (see Figure 7, solid green and red vectors), which means that it is not possible to distinguish the TPEF signal of elastin and calcification. Similar observations were made for the green (525/50 nm) detection channel (data not shown). We also inspected a dark-red filter (650/50 nm), where we could still detect elastin, but the signal level was too low for quality imaging. For calcification, no signal was detected in this spectral range (data not shown). Considerable differences were experienced in case of the Phloxine B stained, deparaffinized sections for elastin and calcification (see Figure 7, dashed green and red vectors). The color vector of elastin is still high in the cyan channel, but it exhibits a

considerable decrease in the orange channel. In opposition, color vector of calcification displayed a prominent shift towards the orange spectrum and its value considerably dropped in the cyan detection channel.

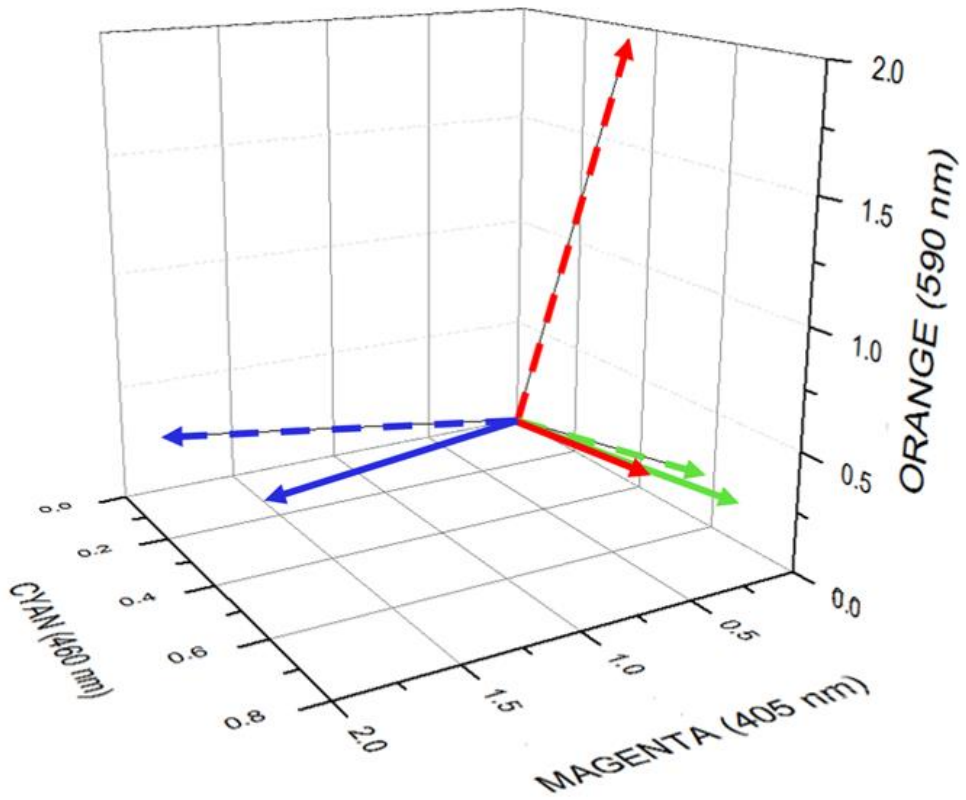

Figure 7. Color vectors of gain-normalized nonlinear optical signals of collagen, elastin and calcification measured in three emission channels. Solid vectors indicate vector coordinates of PXE cryosection, dashed vectors refer to the mean of color vector coordinates of Phloxine B stained PXE sections. Vectorial endpoints correspond to values listed in Table 4. Colors codes: collagen (blue), elastin (green) and calcium deposits (red). Axis labels refer to central wavelengths of the applied bandpass filters before the NDD detectors [101].

3.2.2 Emission filters for three-channel PXE measurements

Based on our results from the previous section, an SHG (405/20 nm) filter was chosen for collagen detection, a cyan (460/50 nm) filter was applied for the NLM imaging of

elastin and an orange (590/45 nm) filter for calcification. As two detection channels are at disposal simultaneously in our imaging apparatus, two measurements were performed for each sample. First, we used a SHG paired with the orange filter and then a cyan bandpass filter paired with the orange filter. Exact spatial overlapping of the corresponding images were ensured with the orange images.

3.2.3 Inverse matrix calculation and three-channel decomposition

As mentioned earlier, we experienced that emission spectra of elastin and calcium deposits can not be separated in a four color (viola/cyan/green/orange) vectorial space in frozen PXE sections. However, the application of low concentration Phloxine B solution after the deparaffinization process evoked beneficial spectroscopic changes. TPEF signal of elastin remained most intensive in the cyan channel, whereas calcification exhibited an enlarged TPEF signal captured with the orange bandpass filter. As a consequence, elastic fibers and calcium deposits could be optically distinguished based on their TPEF spectra. Panel A of Figure 8. displays reference images that were analysed to determine inverse matrix coefficients. To demonstrate the calculation of the inverse matrix, coefficients from patient 2 are substituted into Eq. (1), so as to obtain a transfer matrix [A] for the Phloxine B stained PXE section (Eq. (2)), from which, an inverse matrix [A]−1 was derived (Eq. (3)).

$$\begin{bmatrix} I_{405(x,y)} \\ I_{460(x,y)} \\ I_{590(x,y)} \end{bmatrix} = \begin{bmatrix} a_{405,Co} & a_{405,E} & a_{405,Ca} \\ a_{460,Co} & a_{460,E} & a_{460,Ca} \\ a_{590,Co} & a_{590,E} & a_{590,Ca} \end{bmatrix} \begin{bmatrix} C_{Co(x,y)} \\ C_{E(x,y)} \\ C_{Ca(x,y)} \end{bmatrix} \quad \text{(Eq.1)}$$

$$\begin{bmatrix} I_{405(x,y)} \\ I_{460(x,y)} \\ I_{590(x,y)} \end{bmatrix} = \begin{bmatrix} 0.991 & 0.066 & 0.044 \\ 0.215 & 0.808 & 0.221 \\ 0.136 & 0.176 & 0.997 \end{bmatrix} \begin{bmatrix} 1 \\ 1 \\ 1 \end{bmatrix} \quad \text{(Eq.2)}$$

$$\begin{bmatrix} C_{Co(x,y)} \\ C_{E(x,y)} \\ C_{Ca(x,y)} \end{bmatrix} = \begin{bmatrix} 1.029 & -0.078 & -0.028 \\ -0.247 & 1.318 & -0.280 \\ -0.097 & -0.222 & 1.056 \end{bmatrix} \begin{bmatrix} I_{405(x,y)} \\ I_{460(x,y)} \\ I_{590(x,y)} \end{bmatrix} \quad \text{(Eq.3)}$$

As reflected in the values of the inverse matrix, SHG signal of collagen is captured with a narrowband filter, which results in a minimal contribution of elastin and calcification TPEF to the SHG signal. Conversely, collagen emits low TPEF signal that emerges in the

cyan and orange channels too. Despite the considerable diversion of elastin and calcification color vector in case of Phloxine B stained sections, these two tissue components still emit wide TPEF spectra and contribute with relatively high coefficients to the other cyan or orange channels, respectively. Spectral decomposition executed as an image post-procession with the obtained inverse matrices enabled us to separate optical signals originating of the three tissue components. Crosstalk of overlapping emission spectra was substantially decreased. In the output images, colors refer to the actual chemical concentration of the given tissue component at each pixel. Individual channels of reference images after spatial decomposition and composite of references images before and after decomposition from patient 2 are shown in Figure 8A. Reference images before and after decomposition in patients 3-5 are displayed in Figure 8B. To achieve a different optical contrast, we applied an artificial blue, green, red (RGB) color coding to visualize collagen, elastin and calcification, respectively, that also highlighted co-localization of calcium deposits and elastic fibers.

DOI:10.14753/SE.2023.2777

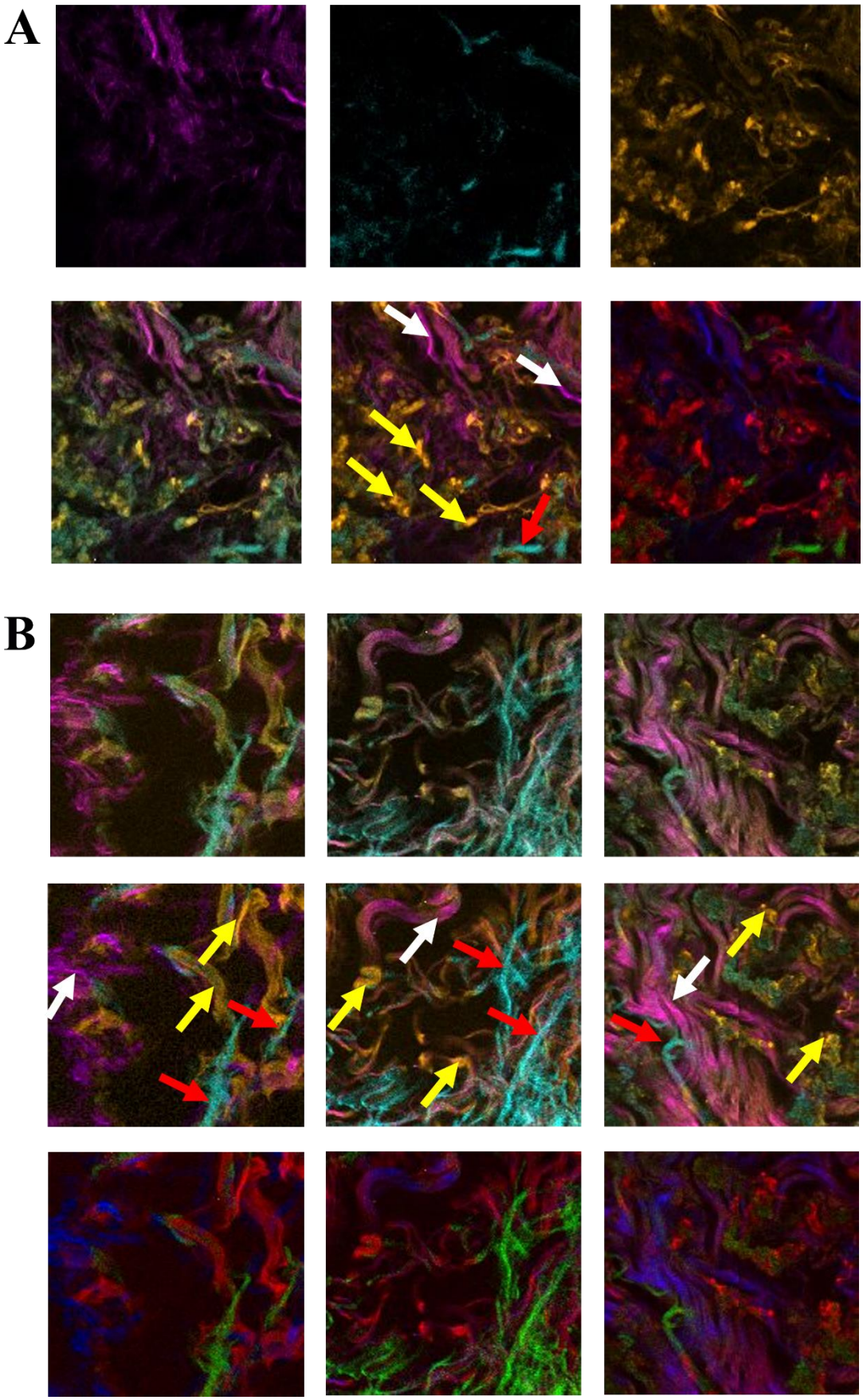

Figure 8. Spectral decomposition of Phloxine B stained PXE sections. (A) First row: representative collagen-, elastin- and calcium deposit-rich areas, respectively, after spectral decomposition in patient 2 in their corresponding three emission channels (405/20 nm, 460/50 nm and 590/45 nm from top to bottom), respectively. Color intensities in these channels were modified based on the retrieved inverse matrix coefficients shown in Eq. 3. These images reveal the actual amounts of collagen, elastin and calcification present, respectively. Second row: Composite of three channels from the first column before (left) and after (middle) spectral decomposition and RGB color coding (right) after decomposition. (B) Composite images of one representative area from patient 3 (left column), patient 4 (middle column) and patient 5 (right column) unprocessed (top), after spectral decomposition (middle) using their corresponding inverse matrix coefficients and RGB color coding (bottom) after decomposition (red: calcification, green: elastin, blue: collagen). White arrow: collagen fibre, red arrow: elastic fibre, yellow arrow: calcium deposits. Reference image size is 132 x 132 μm^2 [101].

3.2.4 NLM imaging and histopathology

In three-color composite mosaic image of the fresh-frozen PXE from patient 1, elastin and calcification exhibit a homogenous light-green color (see Figure 9A), which is the addition of the cyan and orange colors emitted by both. Due to the similar color vectors of elastin and calcification in the PXE cryosection, spectral decomposition resulted in empty black areas in those locations occupied by elastin and mineral deposits, as a consequence of subtraction. Phloxine B stained PXE section from patient 2 without any post-procession is seen in Figure 9B. The effect of Phloxine B staining is explicit in the 3D vectorial space and also in the raw images, where elastin and calcification can already be distinguished based on their color, although spectral overlap in their TPEF signal is still present. The outcome after spectral decomposition of composite image Figure 9B is displayed in Figure 9C. One can notice that spectral decomposition of this mosaic image enabled us to separate connective tissue fibers collagen and elastin, that compose the dermis predominantly. Furthermore, the optical contrast between TPEF signal of elastin and mineral deposits is substantially enhanced. Regions which are affected by calcification became clearly delineated. The epidermis and papillary dermis was not

affected in the NLM images. In the mid-dermis, elastic fibres were fragmented and clumped. Calcification revealed by the TPEForange channel affected extended areas in the mid-dermis and displaced shredded elastic fibers. Mineralized elastic fibres could also be observed. Finally, artificial red, green and blue colors were applied after spectral decomposition in order to reveal calcified elastic fibers (Figure 9D). With routine H&E staining of histopathology sections, the epidermis, the papillary and deep layers of the dermis was intact in all PXE patients. WE stain revealed shredded, polymorphous elastic fibers (Figure 9E). With VK staining, calcium deposits and calcified elastic fibers were displayed (Figure 9F).

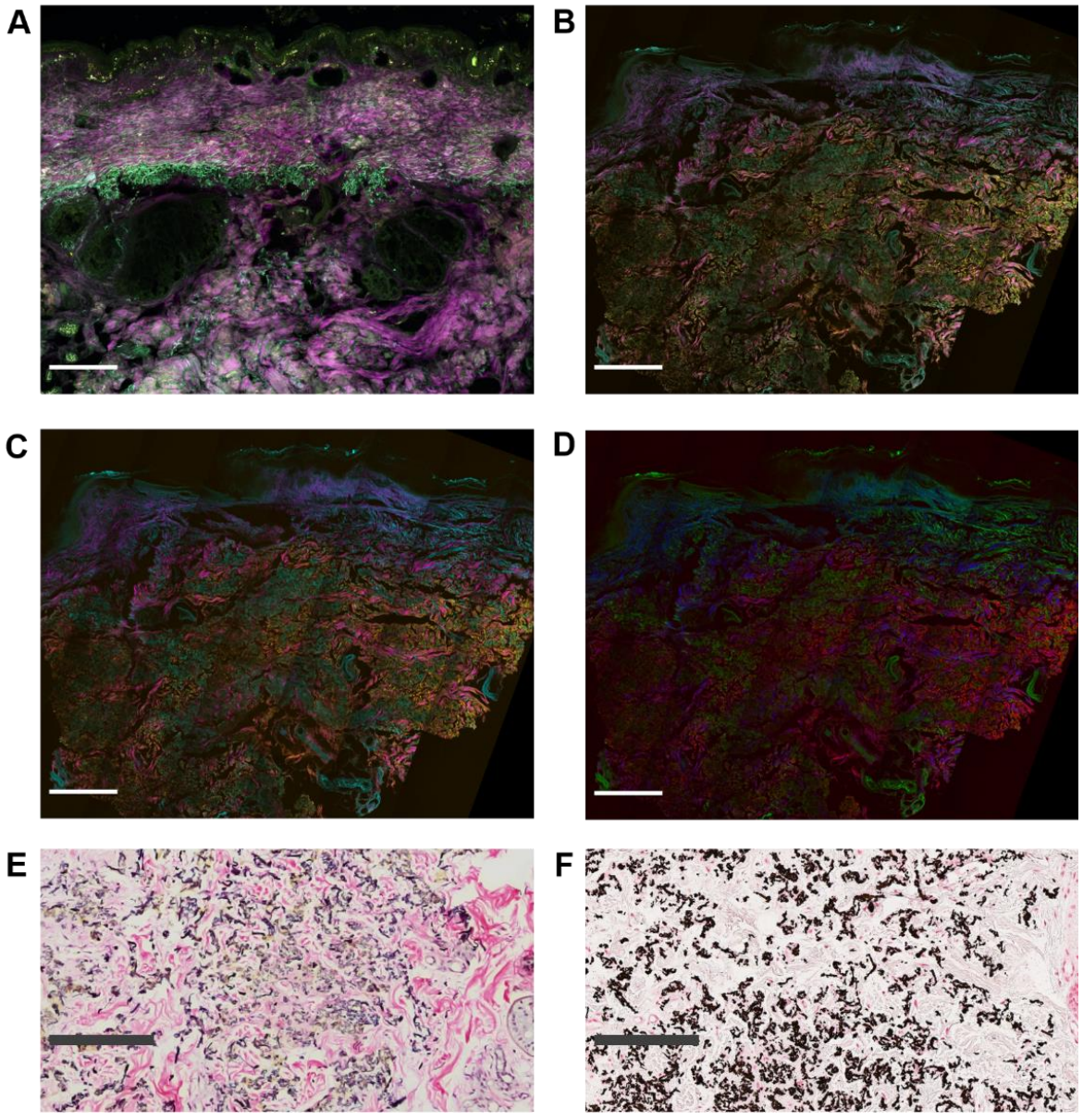

Figure 9. Composite mosaic images of two-photon excitation fluorescence (TPEF) and second-harmonic generation (SHG) signal of PXE-affected skin cryosection, Phloxine B stained PXE section and corresponding histopathology images. PXE cryosection of patient 1 (A), Phloxine B stained, deparaffinized PXE skin sections of patient 2 (B-D) and histopathological sections from patient 2 (E-F). TPEF signals originating from elastin and calcium deposits were captured with a cyan (460/50 nm) and an orange (590/45 nm) emission filter, respectively. Collagen SHG signal was spectrally separated by a 405/20 nm bandpass filter and displayed in magenta. Keratin in the epidermis has contribution to the orange, and to some extent, to the cyan channel. Individual field of views of 420 × 420 μm^2 were assembled into mosaic images (A-D). (A) Patient 1. Composite mosaic image of $TPEF_{cyan}$, $TPEF_{orange}$ and SHG signals in fresh-frozen PXE cryosection. (B-D) Patient 2. Composite mosaic images of a Phloxine B stained, deparaffinized PXE section. (B) Composite mosaic image of $TPEF_{cyan}$, $TPEF_{orange}$ and SHG signals. (C) Composite of $TPEF_{cyan}$, $TPEF_{orange}$ and SHG mosaic images after decomposition with inverse matrix described in Eq.3. (D) Artificial red, green and blue color coded mosaic image of the (C) composit image(red: calcification, green: elastin, blue: collagen). Scale bar displays 400 μm. (E-F) Patient 2. Histolopathology images of the mid-dermis, stained with Weigert's elastic (E) and von Kossa (F) staining. Scale bar displays 200 μm [101].

4. Discussion

The complex nature of PXE determines the natural flow of the disease and influences the risk of the individual patient to develop multiorgan disfunction. Several genotypic alterations including causal gene mutations, functional polymorphisms, small effect variants, together with methylation patterns, miRNAs, epigenetic and environmental factors lead to the diverse phenotypic appearance of PXE. Studies that attempt to give insights into the natural history of PXE are scarce [102]. Although pathogenetic factors that accurately determine the disease severity are yet to be identified, parameters that show correlation with the overall clinical status of the patients are now pointed out. These parameters could be used in the future in personalized medicine, to predict the complications of the individual patient at the time of diagnosis and manage them according to their specific risk profile [103]. 18F-NaF and 18F-FDG uptake, plasma PPi level, inflammatory markers, the number of affected skin sites, Phenodex score and ABCC6 variants were all investigated as potential biomarkers of disease activity and severity, but their clinical relevance is limited [90, 104, 105, 106]. Among the above-mentioned factors, plasma PPi levels were reported to be about 50% lower in PXE patients than in healthy controls [82, 107]. When we looked at this parameter, a marked decrease was found; that is in line with data from the literature [108]. One must note, however, that the normal value in healthy individuals falls into a wide range [109]. Also, different techniques have been proposed in the literature to measure PPi level, and the lack of standardized methods yet hampers the rationale of its application in the daily clinical routine.

Given the huge heterogeneity of the symptoms and their temporal onset, the diagnosis often comes delayed, to be only made after an irreversible organ damage. This highlights why early diagnosis is important and complex multidisciplinary care needs to be initiated for patients. As subtle skin alterations are usually the first signs of PXE, the responsibility of dermatologists is great. A thorough clinical assessment together with a properly made skin biopsy are the cornerstone of finding patients affected by PXE [110]. Even though the dermatological examination is the key diagnostic criterion, an ophthalmologic assessment may further support the possibility of PXE. Currently, conventional histopathological examination of the skin is the widely applied objective method for the diagnosis of PXE [86]. Therefore, there is an emerging need for alternatives to conventional histopathological analysis.

Although skin is an organ easy to investigate, there are only a few reports on noninvasive assessment of skin calcification. Dermoscopic features of PXE have been described. These include intertwined yellowish-white clumps on background of light purple-red color, along with subtle reticulated vessels [111]. Despite the fact the most common noninvasive imaging technique is dermoscopy, it has its limitations as it only allows insights into the surface of the skin, so calcium deposits cannot be visualized [112]. Other imaging modalities have been tested in the diagnostic algorithm of PXE. Total body high-resolution CT scan is able to show intradermal thickening and calcification in the medial layer of vasculature, if the degree of atherosclerotic is great enough [113]. Radiology findings include small cutaneous calcium deposits, calcified vessels, atherosclerotic plaques, irregularity and narrowing of the vessels [114]. However, no *in vivo* tool with definitive diagnostic power is available so far.

There are some reports on OCT imaging of PXE skin. OCT uses near-infrared light and converts reflectance properties of tissues into greyscale images. The imaging depth of OCT ranges between 1-2 mm. The first case-report found hyporeflective dermal aggregates with peripheral clefts [115]. Another case report showed hyporeflective areas in the mid-dermis and a more superficial signal loss in lax skin areas compared to normal skin [112]. High-frequency ultrasound (HFUS) operating at 20 MHz was found to yield sufficient resolution and so can be used to in the diagnosis of PXE. In a cohort of PXE patients, a characteristic HFUS pattern of PXE skin was successfully determined. This includes focal hypoechoic structures that were also present in areas where no cutaneous changes could be observed with other ways of evaluation [116]. RCM has not been used for the imaging of PXE affected skin so far, although we have data on perforating PXE, where at the areas of transepidermal elimination of disorganized elastic fibers in the papillary dermis appeared as hyperreflective material, and crossection of mineralized elastic fibers resembled as eggs in a basket [117].

In the literature, there is only one study to report the *ex vivo* application of NLM in PXE. SHG and autofluorescence were detected in formalin-fixed PXE skin sections from one single PXE patient. The authors described fragmented elasic fibres with diminished autofluorescence properties. On important shortcoming is that they could not detect calcification with that NLM setup [118]. Recently, the first and yet the only report on *in vivo* application of NLM imaging of PXE-affected skin was published. The

aforementioned MPTflex multiphoton microscopy tomography device was used in this study. The reported imaging depth was 30 μm below the dermoepidermal junction, to reach the upper part of the reticular dermis. In this work shredded and polymorphous elastic fibres were detected, however, this imaging depth was not sufficient to reveal mineral deposition. RCM was also tested during this experiment, but they could not demonstrate the findings reported previously [112].

Until now, we lacked imaging modalities which could be used not only as a diagnostic tool, but also as a screening tool although screening is vital in order to estimate their risk if systemic organ involvement that will likely to develop and to follow-up patients during treatment. The investigation of ectopic calcification in the skin might fulfill these needs. During conventional histopathology, mineralization is revealed by staining, but light microscopy images are not suitable for further objective quantitative analysis. Moreover, the effectivity and specificity of von Kossa and Weigert's elastic stainings to detect calcification are often disputed [119, 120]. Although in publications in the literature skin calcification could not been detected with NLM, cardiovascular research proved the applicability of this technique in the visualization of mineralization. There are several studies, where TPEF was suitable to detect calcium deposition in arterial walls and to follow the growth of calcified nodules in aortic valves *ex vivo* [121, 122].

In our work, we examined two small cohorts of PXE patients with nonlinear optical microscopy to examine skin calcification. First, we set out to address whether NLO modalities are able to visualize dermal features of PXE in *ex vivo* skin samples. In the first experiment, we managed to detect mid-dermal calcification and detrimental changes in the elastic fibres. We could also visualize calcified elastic fibres, a hallmark of PXE. These changes were detected by capturing TPEF signal emitted by the calcified elastic fibres. Also, the extent of mineralization, number and length of elastic fibres were calculated in a semi-quantitative way. Although both elastin and calcification were detected with one bandpass filter, submicron resolution of the images enabled confidential distinction based on differences in their morphology. The extent of calcification showed high variability among PXE patients. The number of elastic fibres was significantly higher, whereas fibre length was significantly lower in PXE patients, compared to healthy controls as expected, due to fibre fragmentation [94]. The introduced numerical analyses of dermal alterations may be utilized in the future as part of a

standardized protocol. Although SHG imaging of collagen is considered to be highly specific and provides higher resolution, the differences we found in collagen fibre length and width are clinically nonsignificant. Given the fact that collagen fibre alterations are aspecific in PXE, we do not advise include this in any diagnostic protocols.

We also investigated the relationship of measured plasma PPi levels and mid-dermal calcification. Although no correlation was found, this might be explained with the small sample size, or due to other factors that have not been taken into consideration – such as the age of the patients or environmental factors. Thus, the applicability of PPi as a potential biomarker of disease activity or severity may not be contradicted.

Our results confirmed that *ex vivo* NLM is able to visualize characteristic changes of the mid-dermis in PXE-affected skin in formalin fixed, paraffin embedded, deparaffinized sections. Based on our findings, NLM visualized the similar features of PXE, that are revealed by conventional histopathological examination during routine diagnostic procedures. Furthermore, we provided high-resolution imaging of these specific alterations of PXE-affected skin. This is especially important when we consider the fact that histological alterations in PXE are present in macroscopically intact skin areas, and also in patients who lack skin signs [95]. Importantly, these subtle alterations are early diagnostic signs of PXE, and they often precede the damage of other organs [86]. As we were able to detect calcium deposits and all histopathological features could be visualized, we believe that our experimental setup is superior to others found in the literature. In practice, NLM images reach a depth of ~200 μm when using a Ti:sa laser for 2P excitation [112]. We have tried to make z-stack imaging on frozen PXE skin biopsies to find that our imaging depth of ~200 micron is not suitable for *in vivo* imaging of calcification since it is located ~400 micron or more below the skin surface. However, our results indicate the possibility of an easy *ex vivo* diagnostic method by stain-free laser-scanning NLM imaging.

Although histopathological hallmarks of PXE were identified on two-channel NLO images of stain free skin sections orthogonal to the skin surface, elastin and calcification were detected with the same green (525/50 nm) bandpass filter and their differentiation was made solely based on their morphology. This might be challenging for a non-expert eye. The above-mentioned studies in the literature did not apply different bandpass filters to detect calcification, either. Thus, there is an emerging need for optical differentiation

of elastin and calcium deposits with NLM. This method, if the goal is achieved, could be later utilized to differentiate PXE from PXE-like diseases or in the diagnosis of other diseases with cutaneous calcification. Also, quantitative assessment of the calcification could serve as a biomarker to describe the clinical status of patients.

In our second experiment, we investigated nonlinear optical signal properties of collagen, elastin and calcification, the main tissue changes in the dermis in PXE affected skin with three different bandpass filters, that best matched their emission spectra. In case of fresh-frozen cryosection of PXE– and similarly in case of unstained, deparaffinized sections - we found a broad, overlapping emission spectra that arises from elastin and calcification. Similar results were previously described in the literature [123]. Characterization of their emission spectra with gain-normalized signal intensity vectors suggested, that the optical distinction of elastin and mineralization is not possible. In the literature, fluorescent properties of histological stains are reported. Recently, eosin was used to stain PXE skin sections and their fluorescent properties were examined [124]. We applied a low concentration Phloxine B staining after the deparaffinization process, to avoid intense TPEF emission, that would oppress NLO signal arising from other tissue components. Upon this artificial staining, we observed, that emission spectra of elastin and calcification diverged, and their TPEF signal could be measured with different bandpass filters. Thus, it became possible to optically separate these two components of the dermis by laser scanning nonlinear optical microscopy. Also, low concentration stain means low absorption of the laser beam, so tissue damage was avoided. Mineral deposits in PXE-affected skin mainly consist of calcium hydroxyapatite and calcium hydrogen phosphate. Calcification was previously described to exhibit TPEF signal, and its spectrum highly overlaps with elastin emission spectrum [123]. According to recent spectroscopic studies, pure calcium hydroxyapatite does not absorb, nor emit fluorescent light, which is in accordance with its physical characteristics, that it is a white material [125]. Findings from our experiments regarding the indistinguishable fluorescent spectra of elastin and calcium deposits if no contrast agent is applied, is supported by these spectroscopic data. As in PXE calcium is deposited within and around the elastic fibres, it is probable, that fluorescence signal of mineral deposits arises from the remnants of elastin in them. Thus, fluorescent properties of calcification in PXE exhibits similar – if not the same – fluorescence absorption and emission properties as elastin, that is consistent with our

findings. In our second experiment however, we found that Phloxine B strongly stained calcification, spectrally shifted, and increased its TPEF signal in the orange spectrum. Phloxine B is a derivative of fluorescein, a naturally occurring stain. It is a red acid dye, and binds to acidophilic tissue components that are positively charged [126]. Calcium is a strong base ion, therefore it binds Phloxine B. Phloxine B is used similarly as eosin, together with hematoxylin as part of the routine histopathological examination, as their chemical properties are similar [126, 127]. The application of low concentration eosin staining after deparaffinization may lead to similar results, nonetheless this needs further investigation. In our experiments, we found Phloxine B to be applicable to create optical contrast between TPEF signal elastin and calcification. Consequently, we managed to create a contrast between their emitted TPEF signal in Phloxine B stained PXE sections with NLM, although we still experienced an overlap. To create images suitable for quantitative analysis, further characterization of these signals is necessary, that may involve mathematical approaches. *Neher et al.* introduced a nonnegative matrix factorization algorithm to detect and separate the signal of multiply labelled fluorescence images [68]. Three-component decomposition (or unmixing) was already used in SRS microscopy [128]. There have been previous efforts to distinguish NLO signal of calcification in other clinical contexts. *Gade et al.* developed a methodology for simultaneous detection of collagen, elastin and calcification using multiphoton microscopy. Calcification in this experiment was marked with a red fluorescent tracer [122]. *Baugh et al.* studied calcified aortic valve and distinguished mineralization associated fluorescence from that of collagen, by capturing the entire TPEF emission spectra and decomposing it into two components using spectral un-mixing through non-negative matrix factorization [121]. In order to enhance the optical contrast in our second experiment, we developed an inverse matrix-based algorithm to carry out spectral decomposition. Thereby, we were able to create three-color mosaic images, where the different colors indicate the presence and the actual concentration of collagen, elastin and calcification in PXE-affected skin. These images with spectrally separated signals have also clearly shown histological features of PXE. Furthermore, we noticed, that NLM images are sharper, and fine alterations, such as the structure of calcium deposits and disruption of elastic fibers are visualized with greater detail, in comparison to standard histopathology, where the images become blurrier at high magnifications and the

differentiation of the tissue components are more challenging. Moreover, in contrast to histopathology, spatial separation of elastin and calcification became possible based on their optical signal with NLM. An incremental advantage of our method is that it is suitable for quantitative analysis of mid-dermal calcium deposition, the pattern of calcification or the extent of elastic fibre fragmentation.

Our results contribute to a field less developed both from dermatological and optical aspect. The application of NLM in PXE opens new possibilities in the diagnosis and follow-up of PXE patients. As for now, NLM techniques allow a penetration depth of 200 μm below the skin surface, which is the level of the papillary dermis, detection of calcium deposits is rather challenging if not possible, as we mentioned earlier. Although in our experiments we applied *ex vivo* NLM, non-invasive laser-scanning imaging is expected to be available in the future, as the imaging depth of NLM is improving. [129]. If penetration depth of NLM can be increased to ~400-500 μm in the future, creating 2D „optical biopsies" parallel with the skin surface could become an alternative to skin biopsy and conventional histopathology which would decrease the disease burden for patients, especially in the case of rare diseases, where patients usually wait for their diagnosis for a prolonged time. Besides, transmission of the laser beam through optical fibers into handheld devices that are capable of NLM imaging would be a convenient tool for clinicians in the future for *in vivo* bedside diagnosis and management of PXE patients, although further studies are needed [130]. Biomarkers that indicate disease severity may also be discovered. In the future, NLM could also be used to monitor treatment response in PXE, however the relationship of skin calcification and the overall severity of PXE is yet to be unraveled. As a wide variety of therapeutic options awaits including gene-therapy [131], there is be an increasing need for new modalities to monitor therapeutic efficacy. The role of NLM may also arise in the future to investigate other diseases with ectopic calcification.

5. Conclusions

5.1 I. Experiment: application of *ex vivo* TPEF and SHG techniques for the examination PXE-affected skin and its differentiation from healthy skin

- To the best of our knowledge, we were the first in the literature, who successfully applied nonlinear optical microscopy methods in PXE patients to identify pathological skin alterations, including calcification in skin sections orthogonal to the skin surface. TPEF was able to visualize not just fragmentation of the elastic fibers, but calcium deposits and mineralized elastic fibers were also visible in PXE-affected skin. These detrimental changes were absent from the skin of healthy individuals, as expected. As we applied one bandpass filter to capture TPEF signal, we distinguished elastin from calcium deposits based on their morphology. SHG, revealed clear morphology of collagen bundles. Our results were compared and validated by conventional histopathological stains, such as H&E, WE, VG and VK stains. Thus, we concluded that nonlinear optical microscopy modalities are suitable to detect connective tissue alterations and calcification present in PXE-affected skin.
- We introduced numerical methods for quantitative and semi-quantitative analysis of PXE specific mid-dermal alterations. We found significantly shorter and higher number of elastic fibres in PXE patients. Although calcification was absent from healthy skin, its relative surface area varied considerably among PXE patients. Collagen fibre length and width was significantly lower in PXE patients, although the difference in these parameters was not considerable.
- Plasma concentration of PPi, a potent inhibitor of mineralization was significantly reduced in PXE patients compared to healthy individuals. In our cohort, PPi did not correlate with the extent of mid-dermal calcium deposition, although other modifying parameters, such as the age of the patients or environmental factors have not been taken into consideration.
- Based on our experiments, *ex vivo* nonlinear optical microscopy was validated as a tool to identify characteristic histopathological alterations in PXE-affected skin in a label-free manner with high resolution. This method might be used in the future in the diagnosis of PXE or to assess skin status of PXE patients. Further

studies are necessitated to determine, if nonlinear microscopy assessment of PXE-affected skin might be used to predict clinical outcome of the disease.

5.2 II. Experiment: High-chemical contrast imaging of PXE-affected skin with *ex vivo* TPEF and SHG techniques

- In our experiments, we created optical contrast between the emitted TPEF signal of elastin and calcification by the application of Phloxine B stain after the deparaffinization process. This was an indispensable step towards the spectral separation of the TPEF signal emitted by elastin and calcification.
- We captured the emitted TPEF and SHG signals of collagen, elastin and calcification by three different bandpass filters. We determined the contribution of these three tissue components to TPEF and SHG signals intensities at each detection channel and carried out spectral unmixing of their overlapping emission spectra. With the applied image procession algorithm, we could considerably increase chemical selectivity and the created three-color mosaic images reflect actual concentration of the dermal tissue components.
- Our results bear incremental benefits compared to conventional histopathology since spectrally unmixed NLM images can be directly used to carry out quantitative analysis on the extent of mid-dermal calcium deposition or to examine the pattern of calcification. Furthermore, fine alterations to elastic fibers could be better identified due to higher chemical selectivity and higher spatial resolution of NLM. In the future, three-channel imaging and spectral unmixing of *ex vivo* deparaffinized PXE skin samples may be used for quantitative analysis during the diagnostics or monitoring of patients. This method could be utilized also in case of other diseases with ectopic calcification.

DOI:10.14753/SE.2023.2777

6. Summary

The medical application of nonlinear optical imaging was a milestone in the expanding field of noninvasive medical imaging. A turning point in the history of nonlinear optical microscopy (NLM) began in the 2000s, when the first commercially available device was launched. Since then, application of NLM is a subject of continuous research. NLM is a promising imaging modality also in dermatology, as it offers the investigation of skin cancers, inflammatory conditions, or even hereditary skin diseases.

Pseudoxanthoma elasticum (PXE) is a rare, multisystemic disease with autosomal recessive inheritance. During our experiments, we carried out two-photon emission fluorescence (TPEF) and second harmonic generation (SHG) imaging on *ex vivo* skin sections of PXE patients and healthy controls. We identified histopathological hallmarks of PXE, such as fragmented and mineralized elastic fibers and mid-dermal calcium deposition in the PXE samples, which features were absent from healthy skin. We introduced semiquantitative analysis to assess elastic fibers and calcification. Elastic fibre length and number showed significant differences compared to healthy skin. The area affected by calcification varied among PXE patients. Plasma inorganic pyrophosphate concentration was also measured in all patients.

In our second experiment, we applied Phloxine B staining after the deparaffinization process to create a strong optical contrast between the TPEF signal of elastin and calcification. We introduced an inverse matrix based mathematical approach, so that the NLO signal of elastin calcification and collagen could be spectrally separated. Thus, we created three-color mosaic images, where colors indicate the presence and represent the actual concentration of the given substance. This algorithm enables the objective morphological assessment and quantitative analysis of PXE skin sections, that is not feasible in feasible in standard hematoxylin and eosin-stained histology sections.

These results could be exploited in the future gain deeper insight in the pathogenesis of PXE or to find cutaneous biomarkers that determine disease severity. Further development of the laser setup is necessary for the *in vivo* application of the presented methods, so that NLM can be used to diagnose or monitor PXE through the skin.

7. References

1. Kownacki S**.** (2014) Skin diseases in primary care: what should GPs be doing? Br J Gen Pract, 64(625): 380-1.
2. Lowell BA, Froelich CW, Federman DG, Kirsner RS**.** (2001) Dermatology in primary care: Prevalence and patient disposition. J Am Acad Dermatol, 45(2): 250-5.
3. Ferreira IG, Weber MB, Bonamigo RR**.** (2021) History of dermatology: the study of skin diseases over the centuries. An Bras Dermatol, 96(3): 332-45.
4. Schneider SL, Kohli I, Hamzavi IH, Council ML, Rossi AM, Ozog DM**.** (2019) Emerging imaging technologies in dermatology: Part I: Basic principles. J Am Acad Dermatol, 80(4): 1114-20.
5. Koehler MJ, Lange-Asschenfeldt S, Kaatz M**.** (2011) Non-invasive imaging techniques in the diagnosis of skin diseases. Expert Opinion on Medical Diagnostics, 5(5): 425-40.
6. Attia A, Bi R, Dev K, Du Y, Olivo M**.** (2020) Clinical noninvasive imaging and spectroscopic tools for dermatological applications: Review of recent progress. Translational Biophotonics, 2.
7. Grand D, Navrazhina K, Frew JW**.** (2019) A Scoping Review of Non-invasive Imaging Modalities in Dermatological Disease: Potential Novel Biomarkers in Hidradenitis Suppurativa. Frontiers in Medicine, 6(253).
8. Zhou L, Fu H, Lv T, Wang C, Gao H, Li D, Deng L, Xiong W**.** (2020) Nonlinear Optical Characterization of 2D Materials. Nanomaterials (Basel), 10(11).
9. Garmire E**.** (2013) Nonlinear optics in daily life. Optics express, 21: 30532-44.
10. Carriles R, Schafer DN, Sheetz KE, Field JJ, Cisek R, Barzda V, Sylvester AW, Squier JA**.** (2009) Invited review article: Imaging techniques for harmonic and multiphoton absorption fluorescence microscopy. Rev Sci Instrum, 80(8): 081101.
11. Verstraete C, Mouchet SR, Verbiest T, Kolaric B**.** (2019) Linear and nonlinear optical effects in biophotonic structures using classical and nonclassical light. J Biophotonics, 12(1): e201800262.

12. Dudley J, Genty G, Coen S**.** (2006) Dudley, J. M., Genty, G. & Coen, S. Supercontinuum generation is photonic crystal fiber. Rev. Mod. Phys. 78, 1135-1184. Rev. Mod. Phys., 78: 1135-84.
13. Theer P, Denk W, Sheves M, Lewis A, Detwiler PB**.** (2011) Second-harmonic generation imaging of membrane potential with retinal analogues. Biophys J, 100(1): 232-42.
14. Naumov AN, Zheltikov AM, Fedotov AB, Sidorov-Biryukov DA, Tarasevitch AP, Zhou P, von der Linde D**.** (2001) Pressure control of phase matching in high-order harmonic generation in hollow fibers filled with an absorbing weakly ionizing gas. Journal of the Optical Society of America B, 18(6): 811-7.
15. del Hoyo J, de la Cruz AR, Grace E, Ferrer A, Siegel J, Pasquazi A, Assanto G, Solis J**.** (2015) Rapid assessment of nonlinear optical propagation effects in dielectrics. Sci Rep, 5: 7650.
16. Huff TB, Shi Y, Fu Y, Wang H, Cheng JX**.** (2008) Multimodal Nonlinear Optical Microscopy and Applications to Central Nervous System Imaging. IEEE J Sel Top Quantum Electron, 14(1): 4-9.
17. Cicchi R, Kapsokalyvas D, Pavone FS**.** (2014) Clinical nonlinear laser imaging of human skin: a review. Biomed Res Int, 2014: 903589.
18. Kiss N, Haluszka D, Lorincz K, Kuroli E, Harsing J, Mayer B, Karpati S, Fekete G, Szipocs R, Wikonkal N, Medvecz M**.** (2018) Ex vivo nonlinear microscopy imaging of Ehlers-Danlos syndrome-affected skin. Arch. Dermatol. Res., 310: 463-73.
19. Zipfel WR, Williams RM, Webb WW**.** (2003) Nonlinear magic: multiphoton microscopy in the biosciences. Nature Biotechnology, 21(11): 1369-77.
20. Boppart SA**.** Stain-Free Structural and Molecular Histopathology using Programmable Supercontinuum Pulses. Optics in the Life Sciences Congress, 2017/04/02 2017. San Diego, California. Optical Society of America: JTu1C.2.
21. Hanson KM, Bardeen CJ**.** (2009) Application of nonlinear optical microscopy for imaging skin. Photochem Photobiol, 85(1): 33-44.
22. Balu M, Zachary CB, Harris RM, Krasieva TB, König K, Tromberg BJ, Kelly KM**.** (2015) In Vivo Multiphoton Microscopy of Basal Cell Carcinoma. JAMA Dermatol, 151(10): 1068-74.

23. Gibson EA, Masihzadeh O, Lei TC, Ammar DA, Kahook MY**.** (2011) Multiphoton microscopy for ophthalmic imaging. J Ophthalmol, 2011: 870879.
24. Benninger RK, Piston DW**.** (2013) Two-photon excitation microscopy for the study of living cells and tissues. Curr Protoc Cell Biol, Chapter 4: Unit 4.11.1-24.
25. König K, Breunig HG, Batista A, Schindele A, Zieger M, Kaatz M**.** (2020) Translation of two-photon microscopy to the clinic: multimodal multiphoton CARS tomography of in vivo human skin. J Biomed Opt, 25(1): 1-12.
26. Ortega S, Fabelo H, Iakovidis DK, Koulaouzidis A, Callico GM**.** (2019) Use of Hyperspectral/Multispectral Imaging in Gastroenterology. Shedding Some–Different–Light into the Dark. J Clin Med, 8(1).
27. So PTC, Dong CY, Masters BR, Berland KM**.** (2000) Two-Photon Excitation Fluorescence Microscopy. Annual Review of Biomedical Engineering, 2(1): 399-429.
28. Szipocs R, Antal PG, Szigligeti A, Kolonics A**.** Tunable, Low Repetition Rate, Femtosecond Pulse Ti:Sapphire Laser for In Vivo Imaging by Nonlinear Microscopy. Optics in the Life Sciences, 2011/04/04 2011. Monterey, California. Optical Society of America: JTuA12.
29. Perry SW, Burke RM, Brown EB**.** (2012) Two-photon and second harmonic microscopy in clinical and translational cancer research. Ann Biomed Eng, 40(2): 277-367.
30. Helmchen F, Denk W**.** Deep tissue two-photon microscopy. Nat. Methods; 2005.
31. Cammarata A, Zhang W, Halasyamani PS, Rondinelli JM**.** (2014) Microscopic Origins of Optical Second Harmonic Generation in Noncentrosymmetric–Nonpolar Materials. Chemistry of Materials, 26(19): 5773-5853.
32. Margulis W, Österberg U**.** (1988) Second-harmonic generation in optical glass fibers. Journal of the Optical Society of America B, 5(2): 312-317.
33. Kim DW, Xiao GY, Ma GB**.** (1997) Temporal properties of the second-harmonic generation of a short pulse. Appl Opt, 36(27): 6788-6880.
34. Damianos D**.** Second harmonic generation (SHG) for contactless characterization of dielectric-semiconductor interfaces; 2018.

35. Cox G**.** (2011) Biological applications of second harmonic imaging. Biophys Rev, 3(3): 131.
36. Macias-Romero C, Teulon C, Didier M, Roke S**.** (2019) Endogenous SHG and 2PEF coherence imaging of substructures in neurons in 3D. Optics Express, 27(3): 2235-2282.
37. Perry SW, Burke RM, Brown EB**.** (2012) Two-photon and second harmonic microscopy in clinical and translational cancer research. Ann. Biomed. Eng.
38. Davoudzadeh N, Ducourthial G, Spring BQ**.** (2019) Custom fabrication and mode-locked operation of a femtosecond fiber laser for multiphoton microscopy. Sci Rep, 9(1): 4233.
39. Shin S, Hur J-G, Park JK, Kim D-H**.** (2021) Thermal damage free material processing using femtosecond laser pulses for fabricating fine metal masks: Influences of laser fluence and pulse repetition rate on processing quality. Optics & Laser Technology, 134: 106618.
40. Voigt FF, Emaury F, Bethge P, Waldburger D, Link SM, Carta S, van der Bourg A, Helmchen F, Keller U**.** (2017) Multiphoton in vivo imaging with a femtosecond semiconductor disk laser. Biomedical optics express, 8(7): 3213-3244.
41. Bueno JM, Ávila FJ, Artal P**.** (2019) Comparing the performance of a femto fiber-based laser and a Ti:sapphire used for multiphoton microscopy applications. Applied Optics, 58(14): 3830-3835.
42. Ducourthial G, Leclerc P, Mansuryan T, Fabert M, Brevier J, Habert R, Braud F, Batrin R, Vever-Bizet C, Bourg-Heckly G, Thiberville L, Druilhe A, Kudlinski A, Louradour F**.** (2015) Development of a real-time flexible multiphoton microendoscope for label-free imaging in a live animal. Scientific Reports, 5(1): 18303.
43. König K, Weinigel M, Breunig HG, Gregory A, Fischer P, Kellner-Höfer M, Bückle R**.** Current developments in clinical multiphoton tomography: SPIE; 2010.
44. Pegoraro AF, Ridsdale A, Moffatt DJ, Pezacki JP, Thomas BK, Fu L, Dong L, Fermann ME, Stolow A**.** (2009) All-fiber CARS microscopy of live cells. Optics express, 17(23): 20700-20706.
45. Konig K**.** (2008) Clinical multiphoton tomography. J Biophotonics, 1(1): 13-23.

46. Weinigel M, Breunig HG, Uchugonova A, Konig K**.** (2015) Multipurpose nonlinear optical imaging system for in vivo and ex vivo multimodal histology. J Med Imaging (Bellingham), 2(1): 016003.
47. Weinigel M, Breunig HG, Darvin ME, Klemp M, Rowert-Huber J, Lademann J, Konig K**.** (2015) Impact of refractive index mismatches on coherent anti-Stokes Raman scattering and multiphoton autofluorescence tomography of human skin in vivo. Phys Med Biol, 60(17): 6881-6979.
48. Fink C, Haenssle HA**.** (2017) Non-invasive tools for the diagnosis of cutaneous melanoma. Skin Res Technol, 23(3): 261-332.
49. Sugata K, Osanai O, Sano T, Akiyama M, Fujimoto N, Tajima S, Takema Y**.** (2015) Evaluation of unique elastic aggregates (elastic globes) in normal facial skin by multiphoton laser scanning tomography. Eur J Dermatol, 25(2): 138-182.
50. Springer S, Zieger M, Koenig K, Kaatz M, Lademann J, Darvin ME**.** (2016) Optimization of the measurement procedure during multiphoton tomography of human skin in vivo. Skin Res Technol, 22(3): 356-318.
51. Koehler MJ, Kellner K, Hipler UC, Kaatz M**.** (2015) Acute UVB-induced epidermal changes assessed by multiphoton laser tomography. Skin Res Technol, 21(2): 137-180.
52. Koehler MJ, Kellner K, Kaatz M, Hipler UC**.** (2016) Epidermal changes during UVB phototherapy assessed by multiphoton laser tomography. Skin Res Technol, 22(4): 437-479.
53. Leite-Silva VR, Sanchez WY, Studier H, Liu DC, Mohammed YH, Holmes AM, Ryan EM, Haridass IN, Chandrasekaran NC, Becker W, Grice JE, Benson HA, Roberts MS**.** (2016) Human skin penetration and local effects of topical nano zinc oxide after occlusion and barrier impairment. Eur J Pharm Biopharm, 104: 140-147.
54. Yew E, Rowlands C, So PT**.** (2014) Application of Multiphoton Microscopy in Dermatological Studies: a Mini-Review. J Innov Opt Health Sci, 7(5): 1330010.
55. Zieger M, Springer S, Koehler MJ, Kaatz M**.** (2015) [Multiphoton tomography]. Der Hautarzt; Zeitschrift fur Dermatologie, Venerologie, und verwandte Gebiete, 66(7): 511-531.

56. Bognar P, Nemeth I, Mayer B, Haluszka D, Wikonkal N, Ostorhazi E, John S, Paulsson M, Smyth N, Pasztoi M, Buzas EI, Szipocs R, Kolonics A, Temesvari E, Karpati S**.** (2014) Reduced inflammatory threshold indicates skin barrier defect in transglutaminase 3 knockout mice. J Invest Dermatol, 134(1): 105-115.

57. Kolonics A, Csiszovszki Z, Toke ER, Lorincz O, Haluszka D, Szipocs R**.** (2014) In vivo study of targeted nanomedicine delivery into Langerhans cells by multiphoton laser scanning microscopy. Exp Dermatol, 23(8): 596-605.

58. Kiss N, Haluszka D, Lorincz K, Kuroli E, Harsing J, Mayer B, Karpati S, Fekete G, Szipocs R, Wikonkal N, Medvecz M**.** (2018) Ex vivo nonlinear microscopy imaging of Ehlers-Danlos syndrome-affected skin. Arch Dermatol Res, 310(5): 463-472.

59. Anker P, Fésűs L, Kiss N, Noll J, Becker K, Kuroli E, Mayer B, Bozsányi S, Lőrincz K, Lihacova I, Lihachev A, Lange M, Wikonkál N, Medvecz M**.** (2021) Visualization of Keratin with Diffuse Reflectance and Autofluorescence Imaging and Nonlinear Optical Microscopy in a Rare Keratinopathic Ichthyosis. Sensors (Basel, Switzerland), 21(4): 1105.

60. Seidenari S, Arginelli F, Bassoli S, Cautela J, Cesinaro AM, Guanti M, Guardoli D, Magnoni C, Manfredini M, Ponti G, Konig K**.** (2013) Diagnosis of BCC by multiphoton laser tomography. Skin Res Technol, 19(1): e297-304.

61. Klemp M, Meinke MC, Weinigel M, Rowert-Huber HJ, Konig K, Ulrich M, Lademann J, Darvin ME**.** (2016) Comparison of morphologic criteria for actinic keratosis and squamous cell carcinoma using in vivo multiphoton tomography. Exp Dermatol, 25(3): 218-229.

62. Dimitrow E, Ziemer M, Koehler MJ, Norgauer J, Konig K, Elsner P, Kaatz M**.** (2009) Sensitivity and specificity of multiphoton laser tomography for in vivo and ex vivo diagnosis of malignant melanoma. J Invest Dermatol, 129(7): 1752-1759.

63. Fink C, Haenssle HA**.** (2016) Non-invasive tools for the diagnosis of cutaneous melanoma. Skin Res Technol.

64. Koehler MJ, Speicher M, Lange-Asschenfeldt S, Stockfleth E, Metz S, Elsner P, Kaatz M, König K**.** (2011) Clinical application of multiphoton tomography in combination with confocal laser scanning microscopy for in vivo evaluation of skin diseases. Exp Dermatol, 20(7): 589-682.

65. Provenzano PP, Eliceiri KW, Keely PJ**.** (2009) Multiphoton microscopy and fluorescence lifetime imaging microscopy (FLIM) to monitor metastasis and the tumor microenvironment. Clin. Exp. Metastasis, 26(4): 357-426.
66. Radosevich AJ, Bouchard MB, Burgess SA, Chen BR, Hillman EMC**.** (2008) Hyperspectral in vivo two-photon microscopy of intrinsic contrast. Opt. Lett., 33(18): 2164-2169.
67. Y Z, F X, Z J**.** (2018) A Cloud Detection Method for Landsat 8 Images Based on PCANet. Remote Sensing 10(6): 877.
68. Neher RA, Mitkovski M, Kirchhoff F, Neher E, Theis FJ, Zeug A**.** (2009) Blind source separation techniques for the decomposition of multiply labeled fluorescence images. Biophys J, 96(9): 3791-3800.
69. Grosberg LE, Radosevich AJ, Asfaha S, Wang TC, Hillman EMC**.** (2011) Spectral characterization and unmixing of intrinsic contrast in intact normal and diseased gastric tissues using hyperspectral two-photon microscopy. PLoS One, 6(5): e19925-e.
70. Haluszka D, Lorincz K, Kiss N, Szipocs R, Kuroli E, Gyongyosi N, Wikonkal NM**.** (2016) Diet-induced obesity skin changes monitored by in vivo SHG and ex vivo CARS microscopy. Biomed Opt Express, 7(11): 4480-4489.
71. Kiss N, Krolopp A, Lorincz K, Banvolgyi A, Szipocs R, Wikonkal N**.** (2018) Stain-free Histopathology of Basal Cell Carcinoma by Dual Vibration Resonance Frequency CARS Microscopy. Pathol. Oncol. Res., 24(4): 927-956.
72. Lorincz K, Haluszka D, Kiss N, Gyongyosi N, Banvolgyi A, Szipocs R, Wikonkal NM**.** (2017) Voluntary exercise improves murine dermal connective tissue status in high-fat diet-induced obesity. Arch Dermatol Res, 309(3): 209-223.
73. Fésűs L, Krolopp Á, Molnár G, Kiss N, Tamás G, Szipőcs R**.** A 20 MHz, sub ps, Tunable Ti:sapphire Laser System for Real Time, Stain Free, High Contrast Histology of the Skin. Biophotonics Congress: Biomedical Optics 2020 (Translational, Microscopy, OCT, OTS, BRAIN), 2020/04/20 2020. Washington, DC. Optica Publishing Group: MTh3A.4.
74. Fésűs L, Wikonkál N, Szipőcs R**.** Numerical Analysis on ex vivo Second Harmonic Generation Images of Collagen Structure of Unstained Basal Cell

Carcinoma Sections. European Conferences on Biomedical Optics 2021 (ECBO), 2021/06/20 2021. Munich. Optica Publishing Group: EW4A.9.

75. Germain DP**.** (2017) Pseudoxanthoma elasticum. Orphanet J Rare Dis, 12(1): 85.
76. Uitto J, Li Q, Jiang Q**.** (2010) Pseudoxanthoma elasticum: molecular genetics and putative pathomechanisms. J Invest Dermatol, 130(3): 661-730.
77. Moitra K, Garcia S, Jaldin M, Etoundi C, Cooper D, Roland A, Dixon P, Reyes S, Turan S, Terry S, Dean M**.** (2017) ABCC6 and Pseudoxanthoma Elasticum: The Face of a Rare Disease from Genetics to Advocacy. Int J Mol Sci, 18(7).
78. Georgalas I, Tservakis I, Papaconstaninou D, Kardara M, Koutsandrea C, Ladas I**.** (2011) Pseudoxanthoma elasticum, ocular manifestations, complications and treatment. Clin Exp Optom, 94(2): 169-248.
79. Kranenburg G, Baas AF, de Jong PA, Asselbergs FW, Visseren FLJ, Spiering W**.** (2019) The prevalence of pseudoxanthoma elasticum: Revised estimations based on genotyping in a high vascular risk cohort. Eur J Med Genet, 62(2): 90-91.
80. Jansen RS, Kucukosmanoglu A, de Haas M, Sapthu S, Otero JA, Hegman IE, Bergen AA, Gorgels TG, Borst P, van de Wetering K**.** (2013) ABCC6 prevents ectopic mineralization seen in pseudoxanthoma elasticum by inducing cellular nucleotide release. Proc Natl Acad Sci U S A, 110(50): 20206-20216.
81. Favre G, Laurain A, Aranyi T, Szeri F, Fulop K, Le Saux O, Duranton C, Kauffenstein G, Martin L, Lefthériotis G**.** (2017) The ABCC6 Transporter: A New Player in Biomineralization. Int J Mol Sci, 18(9).
82. Jansen RS, Duijst S, Mahakena S, Sommer D, Szeri F, Varadi A, Plomp A, Bergen AA, Oude Elferink RP, Borst P, van de Wetering K**.** (2014) ABCC6-mediated ATP secretion by the liver is the main source of the mineralization inhibitor inorganic pyrophosphate in the systemic circulation-brief report. Arterioscler Thromb Vasc Biol, 34(9): 1985-1983.
83. Fleisch H, Russell RG, Straumann F**.** (1966) Effect of pyrophosphate on hydroxyapatite and its implications in calcium homeostasis. Nature, 212(5065): 901-903.
84. Bäck M, Aranyi T, Cancela ML, Carracedo M, Conceição N, Leftheriotis G, Macrae V, Martin L, Nitschke Y, Pasch A, Quaglino D, Rutsch F, Shanahan C, Sorribas V, Szeri F, Valdivielso P, Vanakker O, Kempf H**.** (2018) Endogenous

Calcification Inhibitors in the Prevention of Vascular Calcification: A Consensus Statement From the COST Action EuroSoftCalcNet. Front Cardiovasc Med, 5: 196.

85. Dedinszki D, Szeri F, Kozák E, Pomozi V, Tőkési N, Mezei TR, Merczel K, Letavernier E, Tang E, Le Saux O, Arányi T, van de Wetering K, Váradi A**.** (2017) Oral administration of pyrophosphate inhibits connective tissue calcification. EMBO Mol Med, 9(11): 1463-1532.
86. Marconi B, Bobyr I, Campanati A, Molinelli E, Consales V, Brisigotti V, Scarpelli M, Racchini S, Offidani A**.** (2015) Pseudoxanthoma elasticum and skin: Clinical manifestations, histopathology, pathomechanism, perspectives of treatment. Intractable Rare Dis Res, 4(3): 113-134.
87. Mansour AM, Annesley WH**.** (1998) Comet-tailed drusen of the retinal pigment epithelium in angioid streaks. Eye, 12: 943-946.
88. Plomp AS, Toonstra J, Bergen AA, van Dijk MR, de Jong PT**.** (2010) Proposal for updating the pseudoxanthoma elasticum classification system and a review of the clinical findings. Am J Med Genet A, 152a(4): 1049-1006.
89. Campens L, Vanakker OM, Trachet B, Segers P, Leroy BP, De Zaeytijd J, Voet D, De Paepe A, De Backer T, De Backer J**.** (2013) Characterization of cardiovascular involvement in pseudoxanthoma elasticum families. Arterioscler Thromb Vasc Biol, 33(11): 2646-2697.
90. Legrand A, Cornez L, Samkari W, Mazzella JM, Venisse A, Boccio V, Auribault K, Keren B, Benistan K, Germain DP, Frank M, Jeunemaitre X, Albuisson J**.** (2017) Mutation spectrum in the ABCC6 gene and genotype-phenotype correlations in a French cohort with pseudoxanthoma elasticum. Genet Med, 19(8): 909-925.
91. Navasiolava N, Gnanou M, Douillard M, Saulnier P, Aranyi T, Ebran JM, Henni S, Humeau H, Leftheriotis G, Martin L**.** (2019) The extent of pseudoxanthoma elasticum skin changes is related to cardiovascular complications and visual loss: a cross-sectional study. Br J Dermatol, 180(1): 207-214.
92. Uitto J, Jiang Q, Varadi A, Bercovitch LG, Terry SF**.** (2014) Pseudoxanthoma Elasticum: Diagnostic Features, Classification, and Treatment Options. Expert Opin Orphan Drugs, 2(6): 567-643.

93. Sasso BM, Cintra ML, de Souza EM**.** (2017) Pseudoxanthoma elasticum. Autops Case Rep, 7(4): 18-21.

94. Hosen MJ, Lamoen A, De Paepe A, Vanakker OM**.** (2012) Histopathology of pseudoxanthoma elasticum and related disorders: histological hallmarks and diagnostic clues. Scientifica (Cairo), 2012: 598262.

95. Chassaing N, Martin L, Calvas P, Le Bert M, Hovnanian A**.** (2005) Pseudoxanthoma elasticum: a clinical, pathophysiological and genetic update including 11 novel ABCC6 mutations. J Med Genet, 42(12): 881-972.

96. Finger RP, Charbel Issa P, Ladewig MS, Götting C, Szliska C, Scholl HP, Holz FG**.** (2009) Pseudoxanthoma elasticum: genetics, clinical manifestations and therapeutic approaches. Surv Ophthalmol, 54(2): 272-356.

97. Arányi T, Bacquet C, de Boussac H, Ratajewski M, Pomozi V, Fülöp K, Brampton CN, Pulaski L, Le Saux O, Váradi A**.** (2013) Transcriptional regulation of the ABCC6 gene and the background of impaired function of missense disease-causing mutations. Front Genet, 4: 27.

98. Akali AU, Sharpe DT**.** (2003) Cervical midline Z-plasty revision surgery for pseudoxanthoma elasticum. Br J Plast Surg, 56(3): 289-379.

99. Viljoen DL, Bloch C, Beighton P**.** (1990) Plastic surgery in pseudoxanthoma elasticum: experience in nine patients. Plast Reconstr Surg, 85(2): 233-242.

100. Kiss N, Fesus L, Bozsanyi S, Szeri F, Van Gils M, Szabo V, Nagy AI, Hidvegi B, Szipocs R, Martin L, Vanakker O, Aranyi T, Merkely B, Wikonkal NM, Medvecz M**.** (2020) Nonlinear optical microscopy is a novel tool for the analysis of cutaneous alterations in pseudoxanthoma elasticum. Lasers Med Sci, 35(8): 1821-1850.

101. Fésűs L, Plázár D, Kolonics A, Martin L, Wikonkál N, Medvecz M, Szipőcs R**.** (2022) Low concentration Phloxine B staining for high chemical contrast, nonlinear microscope mosaic imaging of skin alterations in pseudoxanthoma elasticum. Biomedical Optics Express, 13(1): 252-61.

102. Szeri F, Miko A, Navasiolava N, Kaposi A, Verschuere S, Li Q, Terry SF, Boraldi F, Uitto J, van de Wetering K, Martin L, Quaglino D, Vanakker OM, Tory K, Aranyi T**.** (2020) The pathogenic p.(R391G) ABCC6 displays incomplete

penetrance implying the necessity of an interacting partner for the development of pseudoxanthoma elasticum. medRxiv: 2020.11.26.20236489.

103. Vanakker OM, Leroy BP, Coucke P, Bercovitch LG, Uitto J, Viljoen D, Terry SF, Van Acker P, Matthys D, Loeys B, De Paepe A**.** (2008) Novel clinico-molecular insights in pseudoxanthoma elasticum provide an efficient molecular screening method and a comprehensive diagnostic flowchart. Hum Mutat, 29(1): 205.
104. Omarjee L, Mention PJ, Janin A, Kauffenstein G, Pabic EL, Meilhac O, Blanchard S, Navasiolava N, Leftheriotis G, Couturier O, Jeannin P, Lacoeuille F, Martin L**.** (2020) Assessment of Inflammation and Calcification in Pseudoxanthoma Elasticum Arteries and Skin with 18F-FluroDeoxyGlucose and 18F-Sodium Fluoride Positron Emission Tomography/Computed Tomography Imaging: The GOCAPXE Trial. J Clin Med, 9(11).
105. Utani A, Tanioka M, Yamamoto Y, Taki R, Araki E, Tamura H, Miyachi Y**.** (2010) Relationship between the distribution of pseudoxanthoma elasticum skin and mucous membrane lesions and cardiovascular involvement. J Dermatol, 37(2): 130-135.
106. Mention PJ, Lacoeuille F, Leftheriotis G, Martin L, Omarjee L**.** (2018) 18F-Flurodeoxyglucose and 18F-Sodium Fluoride Positron Emission Tomography/Computed Tomography Imaging of Arterial and Cutaneous Alterations in Pseudoxanthoma Elasticum. Circ Cardiovasc Imaging, 11(1): e007060.
107. Kauffenstein G, Yegutkin GG, Khiati S, Pomozi V, Le Saux O, Leftheriotis G, Lenaers G, Henrion D, Martin L**.** (2018) Alteration of Extracellular Nucleotide Metabolism in Pseudoxanthoma Elasticum. J Invest Dermatol, 138(8): 1862-70.
108. Sánchez-Tévar AM, García-Fernández M, Murcia-Casas B, Rioja-Villodres J, Carrillo JL, Camacho M, Van Gils M, Sánchez-Chaparro MA, Vanakker O, Valdivielso P**.** (2019) Plasma inorganic pyrophosphate and alkaline phosphatase in patients with pseudoxanthoma elasticum. Ann Transl Med, 7(24): 798.
109. Russell RG, Bisaz S, Donath A, Morgan DB, Fleisch H**.** (1971) Inorganic pyrophosphate in plasma in normal persons and in patients with hypophosphatasia, osteogenesis imperfecta, and other disorders of bone. J Clin Invest, 50(5): 961-969.

110. Katona E, Aslanidis C, Remenyik E, Csikós M, Kárpáti S, Paragh G, Schmitz G**.** (2005) Identification of a novel deletion in the ABCC6 gene leading to Pseudoxanthoma elasticum. J Dermatol Sci, 40(2): 115-135.
111. Kawashima S, Togawa Y, Miyachi H, Matsue H**.** (2018) Dermoscopic features of pseudoxanthoma elasticum. Clin Exp Dermatol, 43(2): 175-183.
112. Mehrabi JN, Doong J, Lentsch G, Mesinkovska N**.** (2020) Imaging of in vivo pseudoxanthoma elasticum via multiphoton microscopy and optical coherence tomography. JAAD case reports, 6(8): 702-705.
113. Vos A, Kranenburg G, de Jong PA, Mali WPTM, Van Hecke W, Bleys RLAW, Isgum I, Vink A, Spiering W**.** (2018) The amount of calcifications in pseudoxanthoma elasticum patients is underestimated in computed tomographic imaging; a post-mortem correlation of histological and computed tomographic findings in two cases. Insights into Imaging, 9(4): 493-500.
114. James AE, Jr., Eaton SB, Blazek JV, Donner MW, Reeves RJ**.** (1969) Roentgen findings in pseudoxanthoma elasticum (PXE). Am J Roentgenol Radium Ther Nucl Med, 106(3): 642-648.
115. Persechino F, Giordano D, Marini CD, Franceschini C, Ardigò M, Persechino S**.** (2019) Dermoscopy, Optical Coherence Tomography, and Histological Correlation of Pseudoxanthoma Elasticum. Dermatol Pract Concept, 9(3): 209-218.
116. Guérin-Moreau M, Leftheriotis G, Le Corre Y, Etienne M, Amode R, Hamel JF, Croué A, Le Saux O, Machet L, Martin L**.** (2013) High-frequency (20-50 MHz) ultrasonography of pseudoxanthoma elasticum skin lesions. The British journal of dermatology, 169(6): 1233-1241.
117. Nasca MR, Lacarrubba F, Caltabiano R, Verzì AE, Micali G**.** (2016) Perforating pseudoxanthoma elasticum with secondary elastosis perforans serpiginosa-like changes: dermoscopy, confocal microscopy and histopathological correlation. J Cutan Pathol, 43(11): 1021-1024.
118. Murata T, Honda T, Miyachi Y, Kabashima K**.** (2013) Morphological character of pseudoxanthoma elasticum observed by multiphoton microscopy. J Dermatol Sci, 72(2): 199-201.

119. Hernandez-Santana A, Yavorskyy A, Loughran ST, McCarthy GM, McMahon GP**.** (2011) New approaches in the detection of calcium-containing microcrystals in synovial fluid. Bioanalysis, 3(10): 1085-1175.

120. Relucenti M, Heyn R, Petruzziello L, Pugliese G, Taurino M, Familiari G**.** (2010) Detecting microcalcifications in atherosclerotic plaques by a simple trichromic staining method for epoxy embedded carotid endarterectomies. Eur J Histochem, 54(3): e33.

121. Baugh LM, Liu Z, Quinn KP, Osseiran S, Evans CL, Huggins GS, Hinds PW, Black LD, 3rd, Georgakoudi I**.** (2017) Non-destructive two-photon excited fluorescence imaging identifies early nodules in calcific aortic-valve disease. Nat Biomed Eng, 1(11): 914-937.

122. Gade PS, Robertson AM, Chuang C-Y**.** (2019) Multiphoton Imaging of Collagen, Elastin, and Calcification in Intact Soft-Tissue Samples. Current protocols in cytometry, 87(1): e51-e.

123. Fitzmaurice M, Bordagaray JO, Engelmann GL, Richards-Kortum R, Kolubayev T, Feld MS, Ratliff NB, Kramer JR**.** (1989) Argon ion laser-excited autofluorescence in normal and atherosclerotic aorta and coronary arteries: morphologic studies. Am Heart J, 118(5 Pt 1): 1028-1065.

124. Heo YS, Song HJ**.** (2011) Characterizing cutaneous elastic fibers by eosin fluorescence detected by fluorescence microscopy. Ann Dermatol, 23(1): 44-52.

125. Kobayashi T, Nakagawa O, Shirai S, Shimoyama E, Hiruta N, Uchida Y**.** (2017) Fluorescent angioscopic imaging of calcium phosphate tribasic: precursor of hydroxyapatite, the major calcium deposit in human coronary plaques. Int J Cardiovasc Imaging, 33(10): 1455-1516.

126. Rosenbaum R**.** (1947) Phloxine As An Histologic Stain, Especially In Combination With Hematoxylin. Stain Technology, 22(4): 149-201.

127. Wittekind D**.** (2003) Traditional staining for routine diagnostic pathology including the role of tannic acid. 1. Value and limitations of the hematoxylin-eosin stain. Biotech Histochem, 78(5): 261-330.

128. Shi L, Zheng C, Shen Y, Chen Z, Silveira ES, Zhang L, Wei M, Liu C, de Sena-Tomas C, Targoff K, Min W**.** (2018) Optical imaging of metabolic dynamics in animals. Nat Commun, 9(1): 2995.

129. Yasui T, Yonetsu M, Tanaka R, Tanaka Y, Fukushima S-i, Yamashita T, Ogura Y, Hirao T, Murota H, Araki T**.** (2012) In vivo observation of age-related structural changes of dermal collagen in human facial skin using collagen-sensitive second harmonic generation microscope equipped with 1250-nm mode-locked Cr:Forsterite laser. Journal of Biomedical Optics, 18(3): 031108.

130. Krolopp Á, Fésűs L, Szipőcs G, Wikonkál N, Szipőcs R**.** Fiber coupled, 20 MHz Repetition Rate, sub ps Ti:sapphire Laser for in vivo Nonlinear Microscopy of the Skin. In: Boudoux CMKHCWMQKS-KMDNEDCFOLEVMO, Buckley E, eds. Biophotonics Congress 2021, 2021/04/12 2021. Washington, DC. Optical Society of America: DF2A.5.

131. Luo H, Li Q, Cao Y, Uitto J**.** (2020) Therapeutics Development for Pseudoxanthoma Elasticum and Related Ectopic Mineralization Disorders: Update 2020. J Clin Med, 10(1).

8. List of publications

Pulications related to the thesis

Fésűs L, Plázár D, Kolonics A, Martin L, Wikonkál N, Medvecz M, Szipőcs R**.** Low concentration Phloxine B staining for high chemical contrast, nonlinear microscope mosaic imaging of skin alterations in pseudoxanthoma elasticum. **Biomedical Optics Express**. 2022 13(1): 252-61

IF: 3,732

Kiss N, **Fésűs L**, Bozsányi S, Szeri F, Van Gils M, SzaboóV, Nagy AI, Hidvegi B, Szipőcs R, Martin L, Vanakker O, Arányi T, Merkely B, Wikonkál NM, Medvecz M**.** Nonlinear optical microscopy is a novel tool for the analysis of cutaneous alterations in pseudoxanthoma elasticum. **Lasers Med Sci**. 2020 35(8): 1821-30

IF: 3,161

Pulications not related to the thesis

Jobbágy A, Kiss N, Meznerics FA, Farkas K, Plázár D, Bozsányi Sz, **Fésűs L,** Bartha Á, Szabó E, Lőrincz K, Sárdy M, Wikonkál NM, Szoldán P, Bánvölgyi A (2022)
Emergency Use and Efficacy of an Asynchronous Teledermatology System as a Novel Tool for early Diagnosis of Skin Cancer during the First Wave of COVID-19 Pandemic. International journal of environmental research and public health, 19:5 Paper: 2699, 14 p

IF: 4,16

Fésűs L, Jobbágy A, Kiss N, Horváth E, Avci P, Lukács A, Mayer K, Bergler-Czop B, Wikonkál N, Bánvölgyi A (2021)
Dermatologic aspects of bed bug epidemic: An atlas of differential diagnosis. Postepy Dermatologii I Alergologii, 38(2): 184-192

IF: 1,837

Anker P, **Fésűs L,** Kiss N, Noll J, Becker K, Kuroli E, Mayer B, Bozsányi S, Lőrincz K, Lihacova I, Lichacev A, Lange M, Wikonkál N, Medvecz M (2021)
Visualization of keratin with diffuse reflectance and autofluorescence imaging and nonlinear optical microscopy in a rare keratinopathic ichthyosis. Sensors, 21(4): 1105-11

IF: 3,576

Bozsányi S, Farkas K, Bánvölgyi A, Lőrincz K, **Fésűs L**, Anker P, Zakariás S, Jobbágy A, Lihacova I, Lihachev A, Lange M, Bliznuks D, Medvecz M, Kiss N, Wikonkál N (2021)

Quantitative multispectral imaging differentiates melanoma from seborrheic keratosis. Diagnostics, 11(8): 1315-14

IF: 3,706

Farkas K, Bozsányi S, Plázár D, Bánvölgyi A, **Fésűs L**, Anker P, Zakariás S, Lihacova I, Lihachev A, Lange M, Arányi T, Wikonkál N, Medvecz M, Kiss N (2021)

Autofluorescence Imaging of the Skin Is an Objective Non-Invasive Technique for Diagnosing Pseudoxanthoma Elasticum. Diagnostics, 11(2): 260-14

IF: 3,706

Bánvölgyi A, Anker P, Lőrincz K, Kiss N, Márton D, **Fésűs L**, Gyöngyösi N, Wikonkál N (2020)

Smoothened Receptor Inhibitor Vismodegib for the Treatment of Basal Cell Carcinoma: a Retrospective Analysis of Efficacy and Side Effects. J Dermatol Treat, 31(4): 387-398

IF: 3,359

Bánvölgyi A, Lőrincz K, Kiss N, Avci P, **Fésűs L**, Szipocs R, Krenács T, Gyöngyösi N, Wikonkál N, Kárpáti S, Németh K (2020)

Efficiency of long-term high-dose intravenous ascorbic acid therapy in locally advanced basal cell carcinoma - A pilot study. Postepy Dermatologii I Alergologii, 37(4): 548-558

IF: 1,837

Kiss N, Lőrincz K, Medvecz M, **Fésűs L**, Csuha P, Hermányi Zs, Wikonkál NM (2020)

Coronavirus disease 2019 in a psoriatic patient with concomitant chronic obstructive pulmonary disease under treatment with Risankizumab. Dermatol Ther, 33(6):
e14186-2

IF: 2,851

Kiss N, Avci P, Bánvölgyi A, Lőrincz K, Szakonyi J, Gyöngyösi N, **Fésűs L,** Goeun L, Wikonkál N (2019)

Intralesional therapy for the treatment of keratoacanthoma. Dermatol Ther, 32(3): e12872-11

IF: 2,327

Bikov A, Lázár Zs, Horváth P, Tárnoki DL, Tárnoki AD, **Fésűs L**, Horváth M, Mészáros M, Losonczy Gy, Kunos L. Association between serum lipid profile and obstructive respiratory events during REM and non-REM sleep. **Lung.** 2019, 197: 443-450.
IF: 1,817

DOI:10.14753/SE.2023.2777

9. Acknowledgements

At the end of the doctoral thesis, I must express my special thanks and appreciation to those, without whom my scientific work could not have been undertaken.

Firstly, I would like to thank and express my gratitude to my supervisor, Prof. Norbert Wikonkál. I feel lucky, that I was involved in the scientific work of the Photobiology and Photocarcinogenesis Laboratory, as well as I could be a part of the daily life of this constantly improving and cohesive research group. I am honored for the opportunity to engage in research, and for the continuous support, guidance and precious scientific advices that I received during my research work. The optimistic approach and sense of humour of Professor Wikonkál always encouraged me in the difficult times.

I would also like to ecpress my appreciation to my consultant, Dr. Róbert Szipőcs, who made it possible that I could work as an assistant research fellow in the „Femtosecond lasers in nonlinear microscopy" research group of the Wigher Research Centre for Physics for more, than two years. I am grateful, that I could carry out nonlinear microscopic experiments of my doctoral thesis, for his assistance in the experimental execution of my tasks and for his work in the correction of the publications and the thesis. Besides, I could participate in the work in relation to OTKA grant of his research lab, throughout which I learned a lot about the complex, but exciting field of nonlinear optics and laser physics. His help enabled me to gain experimental skills, that were essential for the presented scientific work.

I owe a special debt of gratitude to Dr. Márta Medvecz, for the opportunity to study hereditary dermatological diseases under her guidance in the frame of her OTKA grant. I received continuous support in the feasibility, and precisity, valuable scientific knowledge, useful advices and a lot of care in the and execution of the experiments.

I thank Prof. Miklós Sárdy, that he supported my scientific work as a head of the department and of the doctoral programme. I am grateful for the possibility, that I could continue my research during dermatology training. I would also like to thank Prof. Péter Holló, that he supported my research work during the residency training programme.

I would like to extend my gratitude to my colleagues, who created a pleasant and cheerful working atmosphere under any circumstances. I thank Dr. András Bánvölgyi for his honest support, valuable advices and inspiring scientific ideas. I thank Dr. Kende Lőrincz for the selfless efforts he made any time to contribute to my experiments. I would like to

express my gratitude to Dr. Norbert Kiss, that he was of great help with the implementation and execution of the experiments from organizatory work to technical issues. I benefited a lot from his ideas on new projects. I am grateful to Dr. Antal Jobbágy for the scientific assistance and honest support during my research work. I thank Dr. Dóra Plázár, that she helped me to continue and complete my expriments. I thank Dr. Szabolcs Bozsányi, Dr. Klára Farkas and Dr. Sára Zakariás, that they contributed to the evaluation of the experimental results. I am also grateful to Dr. Pálma Anker, Dr. Fanni Meznerics and other colleagues who have supported me along the way.

I wish to thank Dr. Judit Hársing and Dr. Enikő Kuroli, whose work was indispensable in histopathological evaluation. Besides, I thank the staff of the histology laboratory for the processing of histology samples. I also thank Csilla Szigetvári, who assisted in the preparation of cryosections.

I am grateful to Prof. Miklós Csala, Dr. Tamás Mészáros and Dr. Szilvia Nagy, who were my first supervisors during my student scientific work. Besides learning scholarly curiosity, I received selfless and support and guidance from them to proceed on the scientific path with enthusiasm and perseverance.

I thank to all colleagues and employees of the Department of Dermatology, Dermatooncology and Venerology, Semmelweis University for the opportunity to carry out research work at the clinic.

I am thankful to my friends, with whom I could share all my difficulties. Finally, a special thanks goes to my family, especially to my beloved husband, who encouraged me in every possible way to see the completion of this work.